Characteristics and causes of Deep Western Boundary Current transport variability at 34.5°S during 2009-2014

Christopher S. Meinen[1], Silvia L. Garzoli[2,1], Renellys C. Perez[2,1], Edmo Campos[3,2], Alberto R. Piola[4,5,6], Maria Paz Chidichimo[4,5,6], Shenfu Dong[1], and Olga T. Sato[3]

[1]Atlantic Oceanographic and Meteorological Laboratory, Miami, Florida
[2]Cooperative Institute for Marine and Atmospheric Studies, University of Miami, Miami, Florida
[3]University of São Paulo, São Paulo, Brazil
[4]Servicio de Hidrografía Naval, Buenos Aires, Argentina
[5]Universidad de Buenos Aires, Buenos Aires, Argentina
[6]Instituto Franco-Argentino sobre Estudios de Clima y sus Impactos, Consejo Nacional de Investigaciones Científicas y Técnicas (CONICET), Argentina

Abstract:

The Deep Western Boundary Current (DWBC) at 34.5°S in the South Atlantic carries a significant fraction of the cold deep limb of the Meridional Overturning Circulation (MOC), and therefore its variability affects the meridional heat transport and consequently the regional and global climate. Nearly six years of observations from a line of pressure-equipped inverted echo sounders (PIES) have yielded an unprecedented data set for studying the characteristics of the time-varying DWBC volume transport at 34.5°S. Furthermore, the horizontal resolution of the observing array was greatly improved in December 2012 with the addition of two current-and-pressure-equipped inverted echo sounders (CPIES) at the midpoints of the two westernmost pairs of PIES moorings. Regular hydrographic sections along the PIES/CPIES line confirm the presence of recently-ventilated North Atlantic Deep Water carried by the DWBC. The time-mean absolute geostrophic transport integrated within the DWBC layer, defined between 800-4800 dbar, and within longitude bounds of 51.5°W to 44.5°W is -15 Sv (1 Sv = 10^6 m^3 s^{-1}; negative indicates southward flow). The observed peak-to-peak range in volume transport using these integration limits is from -89 Sv to +50 Sv, and the

temporal standard deviation is 23 Sv. Testing different vertical integration limits based on time-mean water-mass property levels yields small changes to these values, but no significant alteration to the character of the transport time series. The time-mean southward DWBC flow at this latitude is confined west of 49.5°W, with recirculations dominating the flow further offshore. As with other latitudes where the DWBC has been observed for multiple years, the time variability greatly exceeds the time-mean, suggesting the presence of strong coherent vortices and/or Rossby Wave-like signals propagating to the boundary from the interior.

Introduction:

In the South Atlantic at 34.5°S the Deep Western Boundary Current (DWBC) is thought to carry the majority of the cold deep limb of the Meridional Overturning Circulation (MOC) southward toward the Southern Ocean. The MOC system dominates the north-south transport of heat and salt in the Atlantic Ocean (e.g. Trenberth et al. 2001; Ganachaud and Wunsch 2003; Johns et al. 2011), and studies using numerical climate models suggest significant connections between variations in the MOC and changes in societally relevant quantities such as continental precipitation patterns, hurricane intensification, and regional sea level (e.g. Vellinga and Wood 2002; Stouffer et al. 2006; Latif et al. 2007; McCarthy et al. 2015; Lopez et al. 2016). The pathways that the DWBC, and the lower limb of the MOC, take as they pass through the South Atlantic are not as well understood as in the North Atlantic. In a recent paper, Garzoli et al. (2015) used all available WOCE and CLIVAR-era hydrographic sections including dissolved oxygen and chlorofluorocarbon (CFC) data, Argo float profile data, and two different

55 analyses of the Ocean general circulation model For the Earth Simulator (OFES) to trace
56 the time-mean pathways of the DWBC through the South Atlantic. Together with other
57 historical analyses, their results show that the DWBC crosses 5°S as a narrow western
58 boundary current, and it becomes dominated by eddies further south around 8°S-11°S,
59 consistent with earlier mooring observations (Dengler et al. 2004; Schott et al. 2005).
60 Previous work has suggested that when this very energetic eddying flow reaches the
61 Vitória-Trindade Ridge at about 20°S, the mean flow appears to follow two different
62 pathways, with a significant fraction (estimates ranging from 3 to 12 Sv) flowing
63 eastward across the Mid-Atlantic Ridge toward the African continent (e.g. Zangenberg
64 and Siedler 1998; Arhan et al. 2003; Hogg and Thurnherr 2005; van Sebille et al. 2012)
65 and the remainder flowing southward along the western boundary hugging the South
66 American continental slope. The recent analysis of ship sections of CFC, oxygen and
67 salinity by Garzoli et al. (2015) clearly demonstrates that the strongest pathway in the
68 South Atlantic south of about 22°S for recently-ventilated North Atlantic Deep Water
69 (NADW), the primary water mass carried in the DWBC, is along the western boundary in
70 the form of a narrow boundary current similar to what is found in most of the North
71 Atlantic. That study suggests that only a small fraction, about 20%, of the DWBC volume
72 transport flows eastward near 20°S, consistent with Arhan et al. (2003) and van Sebille et
73 al. (2012). The Garzoli et al. (2015) study, however, focused primarily on the time-mean
74 circulation pattern and provides little information about the time variability of the DWBC
75 flow, which is the focus of the present study.
76

77 Variations of the MOC and the DWBC have historically been studied mostly in the North
78 Atlantic (e.g. Meinen et al. 2013a; Perez et al. 2015; Srokosz and Bryden 2015; Frajka-
79 Williams et al. 2016; and citations therein). This has mostly been a matter of
80 convenience and proximity, not a reflection on scientific importance, as theoretical work
81 and numerical models have suggested that variations in the South Atlantic may be critical
82 to the stability and flow of the overall MOC system (e.g. Dijkstra 2007; Drijfhout et al.
83 2011; Garzoli and Matano 2011; Garzoli et al. 2013; Buckley and Marshall 2016). Only
84 in the past few years have observations been collected to study the MOC and/or the
85 DWBC in the South Atlantic region, beginning with repeated upper ocean expendable
86 bathythermograph (XBT) transects (e.g. Garzoli and Baringer 2007; Dong et al. 2009)
87 and full-depth hydrographic sections (e.g. Lumpkin and Speer 2003, 2007; Bryden et al.
88 2011), and later adding continuous moored observations at a few locations including
89 11°S (Hummels et al. 2015) and 34.5°S (Meinen et al. 2012; Meinen et al. 2013b).
90 Gridded data sets from Argo float profiles in the upper 2000 m of the water column and
91 satellite altimetry measurements have also been brought to bear on the meridional flows
92 in the South Atlantic (e.g. Schmid 2014; Dong et al. 2015; Majunder et al. 2016),
93 providing important information about latitudinal variations of the MOC. Note that most
94 of these systems focus only on the volume transport in the upper water column, and do
95 not directly observe the DWBC (e.g. XBT, Argo).
96
97 True continuous time series observations of the time varying deep limb of the MOC, the
98 DWBC, are very limited in the South Atlantic. In terms of continuous measurements of

absolute[1] volume transports, in the scientific literature there are essentially only a few years of observations (2000-2004; 2013-2014) at 11°S (e.g. Hummels et al. 2015), and about one year of observations (2009-2010) at 34.5°S (Meinen et al. 2012). The WOCE Deep Basin Experiment in the early 1990s, used current meters to measure the components of the deep and abyssal flows at 20°S and 30°S with an emphasis on Antarctic Bottom Water (AABW) transports, but did not estimate the integrated DWBC volume transports (Hogg et al. 1999). The purpose of this paper is to extend the DWBC record at 34.5°S to five and a half years (2009-2014), examining daily to monthly changes as well as variability on seasonal and longer time scales. The paper examines possible causes for the largest observed DWBC variations, and puts them into context through comparisons with previous DWBC findings at other latitudes, as well as with numerical model output.

Data and Methods:

The Southwest Atlantic MOC ("SAM") array was first deployed at 34.5°S in March 2009 to capture the meridional flow of the western boundary currents, with the primary aim of making long-term measurements of the western boundary flows associated with the MOC (Meinen et al. 2012; Meinen et al. 2013b). The ultimate long-term goal was also for the SAM array to be a cornerstone for the South Atlantic MOC Basin-wide Array ("SAMBA") at 34.5°S, which is coming to fruition with parallel deployments occurring on the eastern boundary in 2013 and 2014 (e.g. Ansorge et al. 2014). The SAM array

[1] The term "absolute" here refers to transports which include both a 'baroclinic', vertically-sheared, component and a 'barotropic', non-sheared, component. Thus "absolute transport" would include all flow that is operating in a geostrophic manner.

involves four pressure-equipped inverted echo sounders (PIES) deployed at depths ranging from about 1300 m down to about 4700 m, and extending roughly 650 km offshore from the outer edge of the continental shelf (see Table 1 and Figure 1). Note that the Site B PIES (see Figure 1) malfunctioned in 2010 and was lost during a recovery attempt in July 2011, so there is a roughly one-year gap at that site in 2010-2011.

The array location was selected to be just north of the northern edge of the meander window of the Brazil-Malvinas Confluence (e.g. Gordon and Greengrove 1986; Olson et al. 1988; Garzoli 1993; Goni et al. 1996, 2011; Lumpkin and Garzoli 2011) based on altimeter, sea surface temperature (SST), and surface drifting buoy measurements. Depending on the precise indicator of the Brazil-Malvinas Confluence selected, the seasonal movement of the Brazil-Malvinas Confluence is characterized either by meridional shifts centered near 38.5°S (e.g. Matano 1993; Lumpkin and Garzoli 2011) or by pivots around a fixed point located near 39.5°S, 53.5°W, changing its orientation from N-S in austral winter to NW-SE in austral summer (Saraceno et al. 2004). The meridional extremes in the Confluence location (denoted by sharp horizontal SST gradients) are typically found in February and August, as can be seen in SST maps (Figure 1, right panels).

Based on recommendations from the broad South Atlantic Meridional Overturning Circulation (SAMOC) Initiative (see www.aoml.noaa.gov/phod/SAMOC_international/), the PIES array was complemented in December 2012 with two current-and-pressure-equipped inverted echo sounders (CPIES) as part of the parallel South Atlantic MOC-

144 Brazil project ("SAMOC-Br"). These CPIES instruments were deployed near the
145 midpoints of the two westernmost pairs of existing PIES moorings (Figure 1) in order to
146 provide better horizontal resolution across the western boundary currents.
147
148 The analysis of PIES data has become more commonplace within the scientific
149 community over the past few decades, and their use to study the DWBC and the MOC in
150 both the North and South Atlantic has been well documented (e.g., Meinen et al. 2006;
151 Meinen et al. 2012; Meinen et al. 2013a,b). Therefore, the PIES analysis methods will
152 only be summarized here briefly, with the remainder of the methodology details left to
153 the references cited.
154
155 A PIES makes two measurements every hour: 1) the bottom pressure; and 2) the vertical
156 round-trip travel time required for a 12 kHz acoustic pulse to travel from the bottom
157 moored instrument up to the sea surface and back. The bottom pressure measurement is
158 made with a highly precise Paros pressure gauge (e.g. Watts and Kontoyiannis 1990;
159 Donohue et al. 2010), while the round-trip travel time is determined using a transducer
160 and a high quality crystal clock (e.g. Rossby 1969; Watts and Rossby 1977; Tracey and
161 Watts 1986). The travel time measurements from each PIES are calibrated into daily,
162 full-water-column profiles of temperature, salinity and specific volume anomaly via
163 hydrography-derived look-up tables using the Gravest Empirical Mode (GEM) technique
164 (e.g. Meinen and Watts 2000). The application of the GEM method to the PIES in the
165 SAM array was first done in Meinen et al. (2012)[2]; that study demonstrated that the

[2] Note: It was recently discovered that, due to a coding mistake, the time-varying bottom-pressure derived term in the absolute velocity in the 2012 study was added with the incorrect sign. The full time series

166 measured travel times were accurate to roughly 4.4% of the observed range when
167 compared with concurrent CTD profile data. That study also showed that the signal-to-
168 noise ratio (SNR) for the GEM look-up tables was around 20 for depths within the main
169 thermocline/halocline, and decreased to around 1-3 below 2000 dbar. The decreased
170 SNR below 2000 dbar is a result of both a decreased correspondence between the
171 observed changes and the empirical 'mode' captured by the GEM technique, and the
172 much smaller signals themselves at these depths. Because the deep vertical shear (of
173 density as well as horizontal velocity) is generally quite weak in this region – this does
174 not represent a serious limitation for the purposes of this study.
175
176 The combined observations made by an array of PIES are powerful, as when combined
177 with the GEM look-up tables they can provide an estimate of the absolute geostrophic
178 velocity, i.e. the combined baroclinic (vertically-sheared) plus barotropic (depth
179 independent) flow, as follows. Vertically integrating the specific volume anomaly
180 profiles generated from the GEM fields and the PIES travel time measurements yields
181 daily dynamic height anomaly profiles at each of the four instrument sites. Differences in
182 dynamic height anomaly profiles between neighboring PIES sites provide relative
183 geostrophic velocity profiles orthogonal to the line between the PIES (the 'baroclinic'
184 component of the velocity; e.g. Meinen et al. 2006). Differences in bottom pressure from
185 neighboring PIES sites provide absolute geostrophic velocity variability at the bottom
186 that can be used to reference the relative velocity profiles (the 'barotropic' component of
187 the velocity; e.g. Meinen and Watts 2000). Due to the well-known leveling problem, the

---

has been recomputed for the present study. Although the character of the absolute transport time series changes due to this mistake, the major results of the earlier study were not impacted.

188 time-mean absolute geostrophic velocity at the bottom cannot be determined from the
189 bottom pressure differences (e.g. Donohue et al. 2010). The additional measurement of
190 water velocity made by the CPIES can characterize the flow 50 m above the seafloor.
191 However, given that the 2 CPIES were deployed much further apart than the typical
192 velocity decorrelation length scale (e.g. Donohue et al. 2010), and given that there are
193 only measurements at two locations (Figure 1), these velocity observations are too sparse
194 to solve the time-mean absolute velocity reference issue. As such those velocity
195 measurements will not be discussed further in this article, and for the purposes of this
196 study the PIES and CPIES will be treated interchangeably. As time variability is the
197 focus of this paper, the time-mean issue is not crucial for this study. However, to provide
198 reasonable time-mean absolute velocity profiles for discussion, the time-mean velocity
199 from an ocean general circulation model (the model is described in the next section) at
200 1500 dbar was added to the velocity profiles created using the PIES data[3]. Note that only
201 the *time-mean* velocity at only *1500 dbar* is used from the model for this purpose. All
202 time variability from the PIES is independent of the model, as is the time-mean velocity
203 shear profile.
204
205 Most of the detailed testing of PIES-GEM estimated velocities and transports has been
206 done in the North Atlantic where independent estimates were available at concurrent
207 locations – specifically for the DWBC this has been done at 26.5°N (e.g. Meinen et al.

[3] Note that in the earlier Meinen et al. (2012) study the model mean velocity was added near the bottom; however, for this study the model velocity at 1500 dbar was used to avoid the significant ageostrophic velocity components in the model in the nearest-bottom grid cell. The results are not highly sensitive to this choice of reference level. Also the time mean meridional velocities are quite similar if other numerical models are used in place of OFES, e.g. NEMO (see the description of the NEMO run used in Meinen et al. 2013b). For example, the time-mean meridional velocity for the vertical grid cell nearest 1500 dbar, averaged zonally between 51.5°W and 44.5°W, from this NEMO run (-2.4 cm s^{-1}) is very close to the same value for the OFES run (-1.6 cm s^{-1}).

208 2004, 2006, 2013a). Meinen et al. (2013a) compared daily PIES-derived transports to
209 those determined from dynamic height mooring data at 26.5°N and showed that DWBC
210 transports estimated from the two systems had a correlation of r = 0.96, and a root-mean-
211 square difference of 6 Sv. Furthermore, they showed that correlations for baroclinic
212 transports using an assumed level of no motion at 800 dbar were similarly high.
213 Unfortunately there are no independent absolute transport continuous time series
214 measurements for a similar comparison at 34.5°S as there are at 26.5°N. However, it can
215 be noted that the same types of instruments are used for both arrays, and the 34.5°S GEM
216 SNR of ~20 in the main thermocline depth range, and of 1–3 below 2000 dbar, are
217 similar to what is observed at 26.5°N[4].
218
219 The GEM look-up tables used herein are based on a data set of 200 CTD profiles and 365
220 Argo profiles collected before the end of 2008. See Meinen et al. (2012) for more detail
221 and an example GEM look-up table. Since the beginning of the SAM project, quasi-
222 annual CTD sections have been collected along the PIES line both to provide concurrent
223 calibration for the PIES travel times, and to observe finer-scale and better horizontal
224 resolution water mass changes over time. These CTD data have not been incorporated
225 into the GEM fields, and as such they represent an independent data set. For this study,
226 CTD sections from July 2010, December 2010, July 2011, and December 2012 are
227 averaged in a fairly simple manner solely to provide an overview of the major water
228 masses. The CTDs collected right at the PIES sites were also used to calibrate the PIES

[4] Note that, like all bottom pressure gauges, the PIES bottom pressure sensors are subject to exponential and/or linear drift problems. These drifts have been removed via the standard methods (e.g. Donohue et al. 2010) in the analysis presented herein, however variations with periods longer than the record length of each PIES deployment (~4 years) are probably less reliable than variations at shorter periods.

229 measured travel times into the corresponding travel times that would be observed on a
230 common pressure level (e.g. Meinen and Watts, 1998).
231
232 **Numerical model output:**
233 To aid in the interpretation of the observations from the PIES array at 34.5°S, output
234 from a high quality, well-validated, numerical model was also used. The Ocean general
235 circulation model For the Earth Simulator (OFES; e.g., Sasaki et al. 2008) was selected
236 for this study. The OFES model is produced by the Japan Agency for Marine-Earth
237 Science and Technology (JAMSTEC), and it is a massively parallelized implementation
238 of the National Oceanic and Atmospheric Administration/Geophysical Fluid Dynamics
239 Laboratory's Modular Ocean Model version 3 (MOM3). The model equations have been
240 discretized on a Mercator B-grid with 54 vertical z levels and a horizontal resolution of
241 0.1°. For the analysis presented here, model fields were provided by JAMSTEC on 3-day
242 snapshot intervals with a 0.2° horizontal grid (i.e., every other grid point) during the
243 period 1980 through 2006. This roughly 20 km spacing is 5 to 15 times finer than the
244 spacing between the PIES moorings in the real ocean. The OFES model was spun up for
245 50 years using a monthly climatology derived from National Centers for Environmental
246 Prediction-National Center for Atmospheric Research (NCEP/NCAR) reanalysis
247 atmospheric fluxes (Masumoto et al. 2004), and it then was forced with daily mean
248 NCEP/NCAR reanalysis data from 1950 to 2006 (Sasaki et al. 2008). To avoid remaining
249 spin-up transients, only the output from the final 27 years of the run was used for this
250 analysis. This model run was selected because it has previously been validated against

251 both other models and the limited available observations in the South Atlantic (Dong et
252 al. 2011; Perez et al. 2011; van Sebille et al. 2012; Garzoli et al. 2013; 2015).
253
254 **Results and Discussion:**
255 The time-mean absolute velocity section calculated from the PIES data during 2009-2014
256 via the methods described above shows the Brazil Current flowing southward between
257 PIES Sites A and B between the surface and roughly 800 dbar, with the DWBC flowing
258 southward below it (Figure 2a). These flows appear weak and smooth horizontally,
259 however, keep in mind that because these velocities are calculated via the geostrophic
260 method they represent a horizontal average between each pair of PIES sites – i.e.
261 horizontal averages over 2-3 degrees of longitude. Also, along the SAM section west of
262 ~49.5ºW the entire water column flows southward, so there is no obvious separation in
263 the velocity section between the near-surface Brazil Current and the intermediate and
264 deep-water flows. Immediately offshore of these southward flows, recirculations to the
265 north in both the surface and deep layers are observed. Even further offshore, between
266 PIES Sites C and D, the flow turns southward once again.
267
268 The basic structure of the mean velocity section from the OFES model (Figure 2b)
269 compares favorably with the mean section from the data (Figure 2a), albeit with more
270 finely resolved horizontal structure. Additional horizontal information is available from
271 the PIES/CPIES array during the final two years – but before looking at that structure it is
272 instructive to first evaluate the time-mean velocities derived from the original four-PIES
273 array only during the final two-year period (Figure 2c). The roughly 2-year average is

similar to the 4 ½ year average (compare Figures 2a and 2c), with the upper layer recirculation being slightly stronger and the deep ocean recirculation being slightly weaker or even slightly southward at some depths during the shorter 2-year average. Averaging the model velocity output between pairs of PIES to simulate the geostrophic averaging (Figure 2d) yields a section that is qualitatively similar to the 2-year average from the PIES in terms of horizontal and vertical structure, although there are some differences in intensity (compare Figures 2c and 2d).

Including the two CPIES records enhances the horizontal structure of the time-mean section, with a more evident Brazil Current core, a stronger upper ocean recirculation core, and a deep recirculation cell that extends to the bottom (Figure 2e). The model velocity output averaged between the six sites (Figure 2f) is quite similar to the PIES/CPIES velocity section, although the northward recirculation in the model is weaker than observed both near the surface and at depth. An important reminder: The time-mean model velocity at 1500 dbar was used to set the time-mean PIES flow at that pressure level as mentioned earlier (see dashed black lines in Figure 2), so there is perfect agreement between the PIES/CPIES time-mean velocity and the model velocity at 1500 dbar by construction. (Apparent differences at 1500 dbar are contouring artifacts only.)

As noted earlier, at 34.5°S, the western boundary flows in the upper and deep layers (Brazil Current and DWBC, respectively) overlay one another, such that the meridional velocities near the boundary are generally all southward from surface to bottom. One could attempt to use water mass properties to identify the level that bounds the base of

297 the Brazil Current and the top of the DWBC, however as will now be shown, this is not
298 particularly satisfying or successful at this location. Average vertical sections of
299 temperature, salinity, dissolved oxygen, and neutral density (Figure 3) show obvious
300 water mass layers, perhaps most clearly in the dissolved oxygen (Figure 3c). For the
301 purposes of the discussion of deep-water flows in this paper, the following water mass
302 definitions are used following Preu et al. (2013):
303 – Antarctic Intermediate Water (AAIW): salinity less than 34.25 psu;
304 – Upper Circumpolar Deep Water (UCDW): neutral density between 27.75 and 27.90 kg
305 m^{-3} with dissolved oxygen values below 4.5 mL L^{-1};
306 – North Atlantic Deep Water (NADW): neutral density between 27.90 and 28.10 kg m^{-3}
307 with salinity greater than 34.8 psu;
308 – Lower Circumpolar Deep Water (LCDW): neutral density between 28.06 and 28.20 kg
309 m^{-3} with salinity less than 34.8 psu;
310 – Antarctic Bottom Water (AABW): potential temperature less than 0°C.
311 Based on these definitions, the layering of the water column along the SAM array clearly
312 shows AAIW overlaying UCDW, which overlays NADW, which overlays LCDW, which
313 finally overlays the AABW. These are most evident in the oxygen section (Figure 3c),
314 with the enhanced oxygen values of the AAIW around 900 dbar, the NADW around 2800
315 dbar, and the AABW around 4800 dbar standing out from the comparatively lower
316 oxygen waters of the UCDW and LCDW.
317
318 The time-mean locations of the main DWBC water mass interfaces demonstrate some
319 rather surprising results when overlain on the time-mean meridional velocity section

(Figure 4). Very near the continental slope the NADW is carried southward as one would expect in the DWBC, however immediately offshore the entire NADW layer is being carried *northward*, essentially heading back toward the northern formation regions, although the array provides no information on how far to the north these waters are carried beyond 34.5°S. Similarly, all of the time-mean flow that can clearly be tagged as AABW at this section is headed *southward* toward the formation region; this result appears to be robust, as small variations in the time-mean flow added at 1500 dbar from a different model (not shown) would not change these southward values (or the northward sign of the NADW mean recirculating flow). The NADW recirculation is not too surprising, as DWBC recirculations in the NADW layer have been commonly observed at many locations along the DWBC pathway through the Atlantic (e.g., Schott et al. 2005; Johns et al. 2008; Meinen et al. 2012; Hummels et al. 2015). The AABW flow to the south, on the other hand, is somewhat unexpected, as it is counter to both previous hydrographic observations (e.g., Hogg et al. 1999; Mémery et al. 2000) and simple intuition given the location of the formation regions for the AABW.

The historical observations of the flow in this region have primarily been geostrophic estimates relative to an assumed level of no motion, which absolute velocity observations here and elsewhere in the DWBC have called into question (e.g., Meinen et al. 2012; 2013a). The few absolute velocity observations that have been obtained previously in the region, Lagrangian float and direct current meter measurements around 28-30ºS in the Brazil Basin, also found hints of recirculation in both the NADW and AABW layers (e.g., Hogg and Owens 1999; Hogg et al. 1999). There is no question, however, that

343 AABW is observed further north, reaching at least the subtropical North Atlantic in the
344 western half of the Atlantic basin (e.g., Frajka-Williams et al. 2011). The hydrographic
345 observations reported by Coles et al. (1996) provide a possible answer to this conundrum,
346 suggesting a possible interior pathway that would bring AABW to the Vema Channel
347 along the western flank of the Mid-Atlantic Ridge, which would be offshore of the PIES
348 array presented here. The bottom topography contours at AABW depth levels are nearly
349 parallel to the PIES array, which also may complicate capturing an accurate assessment
350 of the deepest flow layers. Another possible reason is simply that two years is
351 insufficient to identify the mean flow; the average velocity over the full five year record
352 between Sites C and D in the AABW layer is very weakly northward (but not statistically
353 significantly different from zero). A detailed analysis of the water masses and their
354 variability is beyond the scope of the present study, and these issues will be revisited in a
355 future manuscript using hydrographic and lowered acoustic Doppler current profiler data
356 that is being collected on recent and near-future cruises. The results shown here do,
357 however, highlight the importance of collecting and interpreting absolute velocities near
358 the boundary, and not just relative velocities.
359
360 *Observed deep flow variability*
361 As has been noted at several other latitudes along the pathway of the DWBC, the
362 temporal variability of the DWBC flow greatly exceeds the time-mean values (e.g. Schott
363 et al. 2004, 2005; Toole et al. 2011; Johns et al. 2008; Send et al. 2011; Hummels et al.
364 2015). The deep flow variability at 34.5°S is no exception (Figure 5). Many/most of the
365 strongest variations in the deep flow within the NADW layer (2000-3200 dbar; right

366 panel in Figure 5) are also observed in the mid-depth and surface layers (center and left
367 panels in Figure 5, respectively). The shear between layers is not constant, however, with
368 some events having similar transport in the NADW layer and the mid-depth layer above
369 (see June 2009 anomalously northward flow event in the middle and offshore parts of the
370 array in Figure 5, center and right panels), while others can be much more intense in one
371 layer than the other (see the anomalously northward flow in the May-June 2012 event and
372 the February-March 2014 event in the offshore parts of the array in Figure 5 where the
373 transport signal in the NADW layer is much larger than in the mid-depth layer
374 immediately above). Interestingly, these intense events in the deep layer are sufficiently
375 large at times that the cumulative NADW flow integrated offshore will reverse sign (see
376 white contours in the right panel of Figure 5), indicating that the offshore recirculation to
377 the north at times exceeds the southward flow of the DWBC itself. In most cases the
378 deep flow, i.e. the flow deeper than 800 dbar, is highly correlated in terms of variability.
379 For example, the transport integrated across the array from Site A to Site D within
380 vertical limits of *either* 800-to-4800 dbar or 2000-to-3200 dbar yields time series that are
381 very highly correlated[5] within one another ($r = 0.98$). For the remainder of the paper,
382 unless otherwise noted the deep transports will be integrated between 800 and 4800 dbar
383 (or between 800 dbar and the seafloor where shallower).
384
385 Integrating the meridional transport through the largest possible DWBC layer, from 800
386 dbar down to 4800 dbar and across the entire array between Sites A and D, it becomes

[5] Some might suspect this high correlation could be artificial due to the calculation of transport via the single 'gravest' mode inherent in the PIES/CPIES analysis technique. While a single 'mode' is used in this manner, a similar correlation analysis of the deep transport integrated in the OFES model yields a very similar high value ($r = 0.95$).

387 clear that these strong events can reverse the deep flow for periods of a few days to a few
388 months (Figure 6, black solid line; see also Table 2 for volume transport statistics)[6]. The
389 resulting time-mean value (-15.2 Sv) is a bit smaller than would be expected given
390 previous moored observations upstream at 11°S (-16.9 Sv for the NADW layer only,
391 Schott et al. 2005; -17.5 Sv for the DWBC, Hummels et al. 2015). It is also a bit smaller
392 than the averages estimated from repeated ship sections at 5°S (e.g. -17.3 Sv; Schott et al.
393 2005, estimated roughly between 800-4800 dbar from their Figure 7a) and at 11°S (e.g. -
394 22.5 Sv; Schott et al. 2005, estimated roughly between 800-4800 dbar from their Figure
395 7b). This lower transport at 34.5°S would be consistent with the Garzoli et al. (2015)
396 pathway analysis that suggests that ~20% of the DWBC transits off toward the eastern
397 side of the basin at around 20°S; note that the Garzoli et al. study used the same OFES
398 model run as one of its analysis tools, so the results are not fully independent from the
399 results presented here. The PIES mean DWBC transport value at 34.5°S is roughly
400 comparable with the widely varying previous estimates of the MOC upper limb at this
401 latitude (e.g. -12.4 Sv from an inverse estimate using hydrographic sections at 32°S,
402 Lumpkin and Speer 2007; -18.1 Sv from repeated expendable bathythermograph sections,
403 Garzoli et al. 2013), as it should be if the bulk of the lower limb of the MOC is carried by
404 the DWBC. However, it must be noted that due to the leveling issue discussed earlier,
405 the time mean calculated herein for the DWBC at 34.5°S is partially dependent on the

[6] Note that the transport integrated over the full record (2009-2014) within the 800-4800 dbar level from Site A to Site D does not use the data from Sites AA and BB, as those two sites are only available during 2012-2014. Because of the sloping topography, the transports integrated with or without Sites AA and BB are slightly different, due to the well-known 'bottom triangle' issue, however the differences are very small. For the period when all sites are available, the transports calculated either with or without Sites AA and BB are correlated with each other with a value of r = 0.97, with a mean difference of 1.4 Sv and a standard deviation of the differences of 5.2 Sv (the standard deviation drops to about 3.8 Sv after a 30-day lowpass filter). The variance associated with the differences between the two transport time series (26.9 Sv^2) represents about 5% of the actual variance in the time series (537.8 Sv^2 without Sites AA and BB; 516.4 Sv^2 with Sites AA and BB).

406 OFES model velocity at 1500 dbar as noted earlier. As such, the time-mean is not the
407 focus here.
408
409 The DWBC variability is demonstrated clearly by the large standard deviation (22.8 Sv)
410 and the wide peak-to-peak range (139.4 Sv; see also Table 2). Even after smoothing with
411 a 30-day low-pass filter, the standard deviation is large (20.8 Sv) and the peak-to-peak
412 range exceeds 95 Sv. These variations are somewhat larger than the ~80 Sv peak-to-peak
413 range observed at 11°S (e.g. Schott et al. 2005; Hummels et al. 2015), however this likely
414 reflects a larger integration domain used at 34.5°S where the array stretches further
415 offshore (~650 km vs. 250 km) and captures more of the DWBC recirculation. As will
416 be shown shortly, integrating the transport at 34.5°S to a roughly similar 200 km distance
417 offshore (i.e. the total longitudinal extent of the 11°S western array) yields smaller peak-
418 to-peak transport of ~60 Sv, which is more comparable with the previous values observed
419 at 11°S.
420
421 The mechanisms behind these large variations will be addressed later in the paper, but
422 before continuing to that topic it is instructive to further characterize the nature of the
423 variations themselves. The transport can be broken into a component relative to an
424 assumed reference level of no motion (e.g. the 'baroclinic', or vertically sheared,
425 component, Figure 6, blue dashed line) and a component associated with the actual
426 reference level velocity (e.g. the 'barotropic', or vertically constant, non-sheared,
427 component, Figure 6, red dash-dot line). The former is calculated here relative to an
428 assumed zero flow at 800 dbar, while the latter is simply the true reference level (800

429 dbar) velocity multiplied by the DWBC integration area. It immediately becomes evident
430 that the transport relative to an assumed level of no motion at 800 dbar (Figure 6, blue
431 dashed line) bears little relationship to the true absolute transport in the DWBC layer
432 (Figure 6, black solid line). The relative contribution to the absolute flow is much
433 smaller than the reference layer contribution, and the two components are statistically
434 uncorrelated with one another ($r = -0.28$). Statistical significance herein is calculated
435 following the methods in Emery and Thomson (1997). The absolute transport is highly
436 correlated with the reference transport ($r = 0.91$), and is not significantly correlated with
437 the relative transport ($r = 0.14$), however that is not to say that the relative contribution is
438 unimportant. While the relative term is typically 10 Sv or less, in some events it greatly
439 exceeds this value, with one event in late 2009 having a southward relative transport
440 exceeding 40 Sv in amplitude for more than a month. In addition to illustrating the fact
441 that the 'baroclinic' term and the 'barotropic' term are uncorrelated, consistent with what
442 has been observed at this location with the first year of data along 34.5°S (Meinen et al.
443 2012) and at other latitudes (e.g. 26.5°N; Meinen et al. 2013a), these results make clear
444 that both the 'baroclinic' and the 'barotropic' terms must be measured directly to quantify
445 the DWBC flow.
446
447 *Spectral distribution of observed DWBC energy*
448 When the first year of data at 34.5°S was published (Meinen et al. 2012), it was not
449 possible to evaluate whether there was an annual cycle in the DWBC transport, although
450 analysis of the OFES model at that time suggested that there was a very weak, albeit not
451 significant, seasonal signal. With nearly five years of real data now available, this can be

452 revisited (Figure 7). With the additional years there is still no obvious annual cycle in the
453 data, even after applying a 30-day low-pass filter to eliminate the higher-frequency
454 signals. The average annual cycle (red line in Figure 7) perhaps hints at a northward
455 anomaly in the first half of the year and a southward anomaly in the second half of the
456 year, consistent with the earlier analysis of the OFES model (Meinen et al. 2012). This
457 observed annual signal is very weak and is highly influenced by other time scales and
458 aliasing. Interestingly, at 26.5°N the pattern is initially the same, as there is no
459 meaningful annual cycle in the DWBC integrated out to ~500 km from the boundary
460 (Meinen et al. 2013a). At 26.5°N, if the DWBC is integrated over a narrower domain
461 spanning only the 'mean' location of the DWBC and not including the recirculations
462 offshore, then an annual cycle is apparent. Following the same idea here for 34.5°S, the
463 annual cycle was explored for the deep transport integrated only between Sites A and B,
464 which spans the 'mean' location of the DWBC at this latitude (see Figure 2). Unlike at
465 26.5°N, there is still no clear annual cycle at 34.5°S even when integrated across this
466 narrower span, and the amplitudes are a factor of 2-4 smaller (not shown). Whether this
467 is a dynamical difference between the two latitudes or merely a sign that additional years
468 of data are needed to tease out the annual cycle at 34.5°S is an area for future research.
469 However, it should be noted that the continuous DWBC record integrated similarly at
470 11°S shows no obvious stable annual cycle either (e.g. Dengler et al. 2004; Schott et al.
471 2005).
472
473 Spectral analysis of the continuous portion (2011-2014) of the absolute transport time
474 series (integrated from Site A to Site D) finds little energy at either the semi-annual or

475 annual periods, with the largest signature being a broad peak spanning periods of 90-160
476 days centered near 145 days (Figure 8; spectra are plotted in variance preserving form, so
477 the area under the curve is proportional to the energy at each period). The relatively short
478 record compared to this time scale results in fairly wide error bars for the spectrum, so
479 the spectral distribution may yield more nuanced results once a few more years of data
480 have been collected. There are noisy spectral peaks in the 20-50 day band. Previous
481 observations focusing on the upper ocean just south of the SAM array (near 37° to 38°S)
482 by Garzoli and Simionato (1990) found wave signals in this same frequency band, which
483 were attributed to both eastward propagating Topographic Rossby Waves (TRWs) and to
484 westward propagating frontal perturbations. The latter are likely to be quite different at
485 34.5°S, which is well outside of the more energetic Confluence region, however the
486 TRWs are quite likely to be present in the region around 34.5°S. Further discussion of
487 the sources of the observed DWBC variations will be presented shortly. Breaking the
488 observed variance into temporal bands (Table 3), the Site A to Site D transport signal
489 clearly has little energy at the semi-annual or annual periods, each representing less than
490 3% of the total variance. The bulk of the energy in the transport time series is at time
491 scales shorter than 170 days. There is a modest amount of energy at time scales between
492 semi-annual and annual, and nearly 15% of the energy is at periods longer than annual in
493 the observed record. Because the record used for the spectral analysis is only a bit over
494 three years long, the analysis of the data likely underestimates the energy available at
495 periods longer than annual. The breakdown by period bands is generally similar when
496 calculated for transports integrated only between Sites A and B (Table 3, parentheses),

497 however the annual and semiannual energy is a bit higher when integrated within that
498 zonal span, despite there being no obvious visual annual cycle.
499
500 *Characterizing the deep flow variations*
501 Characterizing the nature of these flow variations could be approached via Empirical
502 Orthogonal Function analysis (e.g. Emery and Thomson 1997), however the resulting
503 eigenvalues are not statistically significant from one another – i.e. they are 'degenerate'
504 (North et al. 1982) and cannot be physically interpreted in a meaningful way, which may
505 be at least partially due to the relatively short record length. Instead, to characterize the
506 vertical-horizontal structure of these transport variations, composite averages were
507 created based on the transport integrated from 800 to 4800 dbar (or the bottom where
508 shallower) and from Site A to Site D (i.e. the black line in Figure 6). Composite mean
509 sections of meridional velocity were created for 'strong' days, where the southward
510 transport, integrated within the above-described bounds, was greater than the record-
511 length time-mean plus two statistical standard errors of the mean (the standard error was
512 estimated to be 5.2 Sv based on the estimated integral time scale of 17 days; see solid and
513 dashed gray lines in Figure 6), for 'weak days' where the southward transport was less
514 than the record-length time-mean minus two statistical standard errors of the mean, and
515 for 'middle' days with transports within ± two statistical standard errors around the time-
516 mean (Figure 9). Only the time period where the additional instruments at Sites AA and
517 BB were available was used in creating the composites as this provides the best
518 horizontal resolution of data.
519

520 The resulting composites suggest that the anomalous flows have a certain 'barotropicity'
521 inshore of around 49°W, with stronger southward DWBC flows below 1000 dbar
522 corresponding to stronger southward Brazil Current flows above 1000 dbar on 'strong'
523 days, and weaker southward flow in shallow and deep layers on 'weak' days (Figure 9).
524 There is also a hint of an offshore shift of the deep flow on weak days. The zero crossing
525 locations (white contours in Figure 9) seem to be fairly constant in the upper layer, while
526 below roughly 2000 dbar this is not true. By contrast to the apparent 'barotropicity' of
527 the flows near to the continental slope, offshore of around 49°W the composite results
528 suggest significant 'baroclinicity' (i.e. increased vertical shear), with weak northward
529 flow (or even southward flow) at depth but intensified northward flow near the surface on
530 'strong' days, but reduced 'baroclinicity' (i.e. reduced shear) on the 'weak' days. Recall
531 that the definition for 'strong' and 'weak' here is based on the integral of the deep flow
532 across the entire section, so in phase flow anomalies in the deep layer are perhaps an
533 artifact of how the composites are created. Correlation of the deep flows between pairs
534 of PIES/CPIES is quite low, so blending the inshore and offshore deep flows may not
535 provide the clearest separation of events, although integrating the deep flow across the
536 array should in theory provide the best estimate of the 'throughput' of the DWBC by
537 attempting to average out the recirculation offshore. As has been noted in the North
538 Atlantic at 26.5°N however, these recirculations may reach all the way to the Mid-
539 Atlantic Ridge (Meinen et al. 2013a), which if also true at 34.5°S would suggest that
540 some of the recirculation is beyond the range of the array (note that at 34.5°S the Mid-
541 Atlantic Ridge is about 2500 km east of site D).
542

543 To test whether composites based solely on the DWBC flow (and not the recirculation)
544 might produce a clearer picture with regards to the deep inshore and offshore meridional
545 flows, an alternate definition for ‘strong’ and ‘weak’ was developed based only on the
546 deep transport integrated between Sites A and B (Figure 10). The standard deviation of
547 the deep transport variability integrated between Sites A and B is less than half that of the
548 deep transport integrated across the entire array (Table 4), but the peak-to-peak range still
549 exceeds 50 Sv within the narrower span. The statistical standard error of the mean is 1.1
550 Sv, and the integral time scale is about 6 days, suggesting that higher frequencies play a
551 larger role in the observed variability in the narrower span between Sites A and B. The
552 ‘strong’ and ‘weak’ days in the record were again defined as days where the meridional
553 transport experienced southward or northward anomalies greater than two statistical
554 standard errors, respectively. The resulting composites (Figure 11) show similarities to
555 the earlier versions (Figure 9) inshore of about 49°W, with the anomalous flow having
556 significant ‘barotropicity’. The near-slope anomalies are even stronger in these
557 composites, with noticeably stronger flows at all depths on the ‘strong’ days (compare the
558 lower right panels of Figures 9 and 11), and much weaker flows at all depths on the
559 ‘weak’ days (compare the top right panels of Figures 9 and 11). Offshore of 49°W, the
560 composites are quite different from those determined using the Site A to Site D
561 definition. The composites based on the Site A to Site B definition show more
562 ‘barotropicity’ offshore of 49°W, whereas the earlier composites showed more
563 ‘baroclinicity’ (i.e. enhanced shear), particularly on ‘strong’ days. This dichotomy
564 between the two sets of composites suggests two facts about the deep flows: a) the deep
565 near-slope flows are often in phase with the upper layer flows; and b) the deep near-slope

566 flows are often 180° out-of-phase with the deep flows immediately offshore (e.g. when
567 the deep southward flow between the slope and 49°W intensifies, the recirculation to the
568 north between 49°W and 47°W also intensifies). Note that this pattern is also observed in
569 the upper layer, where strong northward recirculations are associated with strong Brazil
570 Current events (Figure 11d).
571
572 This apparent anti-correlation between the deep flow near the slope and the recirculation
573 offshore is somewhat surprising, since as was noted earlier, there is only a very weak
574 correlation between the flow between pairs of PIES. The correlation values between the
575 deep flows integrated in the Site A to Site B span and the deep flows integrated in the
576 Site B to Site C span is about r = -0.4. Based on the average integral time scale for these
577 two records (8 days) and the record length, this correlation value is statistically
578 significantly different from zero at even the 99% level (cutoff r = |0.38|), but a linear
579 relationship between the two would explain less than 20% of the observed variability.
580 Lagged-correlations show insignificant values with a shift of more than a few days in
581 either direction, and this is true for not only the daily records but also for records that
582 have been low-pass filtered (2^{nd} order Butterworth passed both forward and back) with
583 cutoff periods of 10, 30, and 90 days. So while the composites suggest that on average
584 the recirculation offshore intensifies when the southward DWBC flow increases, and vice
585 versa, the actual flow at any given time is more complex and nuanced (e.g. may have
586 shorter spatial scales with banded flow structures). Clearly the deep flow in this region is
587 influenced by many different factors, but the observational array, while well suited to
588 capture the deep meridional transport variability near the western boundary, has limited

589 ability to track deep flow features migrating into the region. Therefore, an evaluation in
590 a numerical model may aid in the interpretation of the observed signals and help extract
591 more information (as was also done in the earlier Meinen et al. 2012 study).
592
593 *Modeled deep flow variability*
594 Integrating the meridional velocity from the OFES model within the same longitude
595 range (between Sites A and D) and over the same pressure range (800 to 4800 dbar or the
596 bottom where it is shallower) using the 27-years of model output yields a robust DWBC
597 with a time-mean similar to the observed value (Figure 12, see also Table 5). While the
598 time-mean values are similar (recall that the model 1500 dbar mean value is imposed on
599 the data, and therefore the means are not completely independent), the time variability
600 from the model is somewhat smaller than that of the real ocean (standard deviation of
601 16.5 Sv versus 22.8 Sv, respectively). As in the real ocean, there is little sign of an
602 annual cycle in the model DWBC transport – perhaps a hint of anomalous northward
603 flow in the first half of the year (Figure 12, lower panel), and anomalous southward flow
604 in the second half, but the variability at other time scales clearly dominates. The
605 percentage of variance explained by the annual or semi-annual periods is less than 10%
606 each (Table 6), although the annual and semi-annual percentage values are a factor of 2-3
607 larger than the comparable values for the observed time series (Table 3). Because the
608 model output record is much longer than the real data set, it is possible to evaluate how
609 much energy is in the longer periods; evaluation both in period bands (Table 6) and as a
610 spectrum (Figure 13) illustrates that the DWBC in the model does not have much energy
611 at periods longer than two years. Even using extended windows for calculating the

612 spectra does not extract much energy at the longer time scales (compare Figure 13 panels
613 b, c, and d). What is clear is that the model variability is weaker than that in the actual
614 observations at essentially all time scales (compare Figure 13a to panels b-d).
615 Nevertheless, the model does show a broad peak of energy centered around 140-160
616 days, just as the observations show, so it is clear that in general the model DWBC has
617 similar, if perhaps too weak, variability when compared to that of the real ocean.
618
619 Having verified that the DWBC variability in the model is qualitatively similar to that in
620 the real ocean (for periods shorter than two years), it is reasonable to then 'step back' and
621 evaluate a larger domain within the model to try and identify the sources/mechanisms
622 behind the variations observed near the continental slope. As a first step toward this goal,
623 a Hovmoller plot of the OFES meridional velocity at the central depth of the NADW near
624 2600 m across 34.5°S between the western continental slope and the Mid-Atlantic Ridge
625 illustrates the presence of waves/eddies propagating both eastward and westward to the
626 west of 40°W (Figure 14). The eastward trending features have propagation speeds of
627 roughly 5-8 cm/s (4.5-7.0 km/day), while the westward trending features west of 40°W
628 have propagation speeds of roughly 3-4 cm/s (2.5-3.5 km/day). East of about 40°W, the
629 flow in the model is dominated by relatively weak features that propagate westward at a
630 much slower speed – roughly 1 cm/s (0.9 km/day). These weaker features do not seem to
631 propagate to the western portion of the basin, although it may be that they are simply
632 obscured by the more energetic, faster features found within approximately 1000 km of
633 the shore. The propagation speeds for the region west of 40°W are in rough agreement
634 with those found in an earlier inverted echo sounder (IES) array located just south of the

635 PIES/CPIES array discussed herein (Garzoli and Simionato 1990). This earlier study
636 found that the eastward propagating signals had the characteristics of TRWs, and given
637 the similar or perhaps even slightly steeper topography in the study region discussed in
638 this study, such a diagnosis seems equally likely here.
639
640 The westward propagating features in the model are consistent with Rossby Wave-like
641 features that have been identified at other latitudes (e.g. Meinen and Garzoli 2014), with
642 propagation speeds that are slightly faster than linear first-mode baroclinic Rossby Wave
643 theory would predict, which is consistent with historical satellite altimeter observations
644 (e.g. Chelton and Schlax 1996; Polito and Liu 2003, Osychny and Cornillon 2004) as
645 well as some recent theoretical work (e.g. Paldor et al. 2007; De Leon and Paldor 2009).
646 Note that some studies point out that these features are in fact more likely "coherent
647 vortices" rather than Rossby Waves, since they are closed circulation features that can
648 translate properties, which waves cannot do (e.g. Chelton et al. 2007). More recently,
649 Polito and Sato (2014) have shown that the dynamics may in fact be a bit more nuanced,
650 presenting evidence that these eddies tend to 'ride' on Rossby Waves.
651
652 The closed nature of these westward propagating features is clear in the model when the
653 model output is viewed as monthly averages. Perhaps the most prominent westward
654 propagating feature in this model run occurs in the latter half of 1987, with a strong clear
655 southward velocity anomaly propagating westward from about 44°W to the boundary
656 (Figure 14). Evaluating monthly averages of the deep velocity in the model at 2600 m
657 depth (i.e. near the core depth for the NADW component of the DWBC) during the last

five months of 1987 and comparing them to the long-term mean velocity easily highlights a closed circulation feature that causes this westward propagating southward velocity anomaly (Figure 15).

The long-term mean from the model (Figure 15a) clearly shows the southward DWBC hugging the continental slope at the latitude of the PIES/CPIES array (yellow line), while in the long-term mean field there is only quite weak circulation in comparison in the offshore portions of the array. The monthly averages from the model for the final five months of 1987 (Figure 15b-f), however, illustrate the highly energetic flows that can be found offshore at any particular time. A strong anticyclonic feature, highlighted by the magenta disc in Figure 15, slowly propagates westward from August through December 1987. The radius of the disc of anticyclonic flow, which was subjectively determined based on the mapped velocities, is roughly 180-200 km for most of the months shown (except for December, Figure 15f, when it drops to around 120 km). The baroclinic Rossby Radius (NH/f, where the Brunt-Väisälä frequency $N = 0.0018\ s^{-1}$ is a typical mid-depth value, the water depth H = 4500 m, and f is the Coriolis parameter) in this area is roughly 100 km in the real world, so about a factor of two smaller than the observed anticyclonic feature. (N.B. – The barotropic Rossby Radius, given by $(gH)^{½}/f$, where g is gravity, is much larger, around 2500 km at this latitude.) As such, referring to these propagating features as 'coherent vortices' is perhaps more appropriate, but some of the features may represent long Rossby Waves (Polito and Sato 2015). Regardless, it is clear that these large westward propagating features are creating the largest transport anomalies in the deep layers in the model, and the correspondence between model and

observations where it can be tested suggests that this is likely true in the real ocean as well.

Conclusions:

As has been found at other locations along the DWBC path through the Atlantic, at 34.5°S the time-varying intensity of the DWBC volume transport during 2009-2014 (22.8 Sv standard deviation, and peak-to-peak range of 139.4 Sv) greatly exceeds the time-mean value (-15.2 Sv) – which illustrates the necessity of continuous observation to avoid aliasing. The spectral character of the observed variability has a broad peak within roughly 90-160 days, centered near 145 days, with additional energy found in the 20-50 day band. Composite analysis (integrated between both Site A to D and Site A to B) suggests that the variations near the continental slope west of 49°W have some 'barotropicity', in the sense that they affect the flow at all layers including those near the sea surface. The composite results also show that the strong southward transport anomalies near the slope are partially compensated by increased recirculation to the north immediately offshore of 49°W, while weak southward transport anomalies near the slope are also partially compensated by decreased recirculation to the north offshore of 49°W.

Coupled with analysis of the time-varying flow along the array and analysis of the broader area in a high-quality, high resolution, well-validated numerical model, the results suggest that the dominant source of transport variations near the continental slope are westward propagating coherent vortices that superimpose on top of and modulate the intensity of the DWBC flow to yield large southward or northward anomalies depending

on the flow associated with the vortices. This suggests that the observing array might be enhanced/improved through the addition of either/both increased horizontal resolution of observations (to more clearly identify these propagating features) and/or the expansion of the array out toward the Mid-Atlantic Ridge (to more completely capture the offshore recirculations). The results also demonstrate the necessity of directly and independently capturing both the 'baroclinic' (vertically sheared) and 'barotropic' (vertically constant) flows in order to properly understand the absolute transport variability of the DWBC at this location.

Acknowledgements:

The authors would like to thank the ship captains and crews of the N.H. Cruzeiro do Sul, A.R.A. Puerto Deseado, S.V. Ice Lady Patagonia II, N.Oc. Alpha-Crucis, and the N.Oc. Alpha Delphini, who have all ably supported our research cruises and project. Ulises Rivero, Rigoberto Garcia, Pedro Peña, Carlos Franca, Marcela Charo, Daniel Valla and the support teams in Miami, São Paulo and Buenos Aires all have helped collect and process the data presented herein. The U.S. PIES/CPIES observations and the participation of CM, SG, RP, and SD were supported via the NOAA Climate Program Office-Climate Observations Division (FundRef number 100007298) under the Southwest Atlantic Meridional Overturning Circulation ("SAM") project, with additional support from the NOAA Atlantic Oceanographic and Meteorological Laboratory. SG and RP were also supported in part under the auspices of the Cooperative Institute for Marine and Atmospheric Studies (CIMAS), a Cooperative Institute of the University of Miami and NOAA, cooperative agreement NA10OAR4320143. RP acknowledges additional support from NOAA (Grant NA13OAR4310131) and NASA (Grant NNX14AH60G). The Brazilian CPIES observations were supported by the São Paulo State Research Foundation (FAPESP) through the SAMOC-Br project (Grant 2011/50552-4). EC acknowledges CNPq for a Research Fellowship (Grant 302018/2014-0). Hydrographic observations were partially supported by the Inter-American Institute for Global Change Research (IAI) grants SGP2076 and CRN3070. The IAI is supported by the US National Science Foundation (grants GEO-0452325 and GEO-1128040). The merged, multi-sensor L4 Foundation sea-surface temperature (SST) data used herein were provided by the NASA Jet Propulsion Laboratory under support from the NASA MEaSUREs program. Rick Lumpkin and Arthur Mariano provided several helpful ideas while the manuscript was being prepared, and Libby Johns, Shane Elipot, and two

anonymous reviewers gave a number of suggestions for improving earlier drafts of the paper.

References:

Ansorge I., M. Baringer, E. Campos, S. Dong, R. A. Fine, S. Garzoli , G. Goni, C. Meinen, R. Perez, A. Piola, M. Roberts, S. Speich, J. Sprintall, T. Terre, and M. van den Berg, Basin-Wide Oceanographic Array Bridges the South Atlantic, *EOS Transactions*, AGU, 95(6), 53-54, 10.1002/2014EO060001, 2014.

Arhan, M., H. Mercier, and Y.-H. Park, On the deep water circulation of the eastern South Atlantic Ocean, *Deep Sea Res. I*, 50, 889-916, doi:10.1016/S0967-0637(03)00072-4, 2003.

Bryden, H. L., B. A. King, and G. D. McCarthy, South Atlantic overturning circulation at 24°S, *J. Mar. Res.*, 69, 39-56, doi:10.1357/002224011798147633, 2011.

Buckley, M. W., and J. Marshall, Observations, inferences, and mechanisms of the Atlantic Meridional Overturning Circulation: A review, *Rev. Geophys.*, 54, 5-63, doi:10.1002/2015RG000493, 2016.

Chelton, D. B., and M. G. Schlax, Global observations of oceanic Rossby Waves, *Science*, 271, 234-238, 1996.

Chelton, D. B., M. G. Schlax, R. M. Samelson, and R. A. de Szoeke, Global observations of large oceanic eddies, *Geophys. Res. Lett.*, 34, L15606, doi:10.1029/2007GL030812, 2007.

Chin, T. M., R. F. Milliff, and W. G. Large, Basin-Scale, High-Wavenumber Sea Surface Wind Fields from a Multiresolution Analysis of Scatterometer Data, *J. Atmos. Ocean. Tech.*, 15, 741–763, 1998.

Coles, V. J., M. S. McCartney, D. B. Olson, and W. M. Smethie Jr., Changes in Antarctic Bottom Water properties in the western South Atlantic in the late 1980s, *J. Geophys. Res.*, 101 (C4), 8957-8970, 1996.

Dengler, M., Schott, F. A., Eden, C., Brandt, P.,Fischer, J., and Zantopp, R., Break-up of the Atlantic Deep Western Boundary Current into eddies at 8°S, *Nature*, 432, 1018–1020, doi:10.1038/nature03134, 2004.

De Leon, Y., and N. Paldor, Linear waves in midlatitudes on the rotating spherical Earth, 39 (12), 3204-3215, doi:10.1175/2009JPO4083.1, 2009.

Dewar, W. K., and J. M. Bane, Subsurface Energetics of the Gulf Stream near the Charleston Bump, *J. Phys., Oceanogr.*, 15 (12), 1771-1789, 1985.

Dijkstra, H. A., Characterization of the multiple equilibria regime in a global ocean model, *Tellus, Ser. A*, 59, 695–705, 2007.

789 Dong, S., S. L. Garzoli, M. O. Baringer, C. S. Meinen, and G. J. Goni, The Atlantic
790 Meridional Overturning Circulation and its Northward Heat Transport in the South
791 Atlantic, *Geophys. Res. Lett.*, 36, L20606, doi:10.1029/2009GL039356, 2009.
792
793 Dong, S., S. L. Garzoli, and M. O. Baringer, The role of inter-ocean exchanges on
794 decadal variations of the northward heat transport in the South Atlantic, *J. Phys.*
795 *Oceanogr.*, 41, 1498–1511, 2011.
796
797 Dong, S. , M. O. Baringer , G. J. Goni , C. S. Meinen , and S. L. Garzoli**,** Seasonal
798 variations in the South Atlantic Meridional Overturning Circulation from observations
799 and numerical models, *Geophys. Res. Lett*., 41, 4611-4618, doi:10.1002/2014GL060428,
800 2014.
801
802 Dong, S., G. Goni , and F. Bringas, Temporal variability of the Meridional Overturning
803 Circulation in the South Atlantic between 20°S and 35°S, *Geophys. Res. Lett.,* 42, 7655 -
804 7662*,* doi:10.1002/2015GL065603, 2015.
805
806 Donohue, K. D., Watts, D. R., Tracey, K. L., Greene, A. D., and Kennelly, M., Mapping
807 circulation in the Kuroshio Extension with an array of current and pressure recording
808 inverted echo sounders, *J. Atmos. Oceanic Tech.*, 27, 507–527,
809 doi:10.1175/2009JTECHO686.1, 2010.
810
811 Drijfhout, S. S., S. L. Weber, and E. van der Swaluw, The stability of the MOC as
812 diagnosed from model projections for pre-industrial, present and future climates, *Clim.*
813 *Dyn.*, 37, 1575-1586, doi:10.1007/s00382-010-0930-z, 2011.
814
815 Emery, W. J., and R. E. Thomson, *Data Analysis Methods in Physical Oceanography*,
816 Pergamon, Oxford, U. K., 1997.
817
818 Frajka-Williams, E., S. A. Cunningham, H. L. Bryden, and B. A. King, Variability of
819 Antarctic Bottom Water at 24.5°N in the Atlantic, *J. Geophys. Res.*, 116, C11026,
820 doi:10.1029/2011JC007168, 2011.
821
822 Frajka-Williams, E., C. S. Meinen, W.E. Johns, D.A. Smeed, A. Duchez, A.J. Lawrence,
823 D.A. Cuthbertson, G.D. McCarthy, H.L. Bryden, M.O. Baringer, B.I. Moat, and D.
824 Rayner, Compensation between meridional flow components of the AMOC at 26°N,
825 *Ocean Sci.,* 12, 481-493, doi:10.5194/os-12-481-2016, 2016.
826
827 Ganachaud, A., and C. Wunsch, Large-Scale Ocean Heat and Freshwater Transports
828 during the World Ocean Circulation Experiment, *J. Clim.*, 16, 696-705, 2003.
829
830 Garzoli, S., and C. Simionato, Baroclinic instabilities and forced oscillations in the
831 Brazil/Malvinas confluence front, *Deep-Sea Res.*, 37 (6), 1053-1074, 1990.
832
833 Garzoli, S. L., Geostrophic velocity and transport variability in the Brazil-Malvinas
834 Confluence, *Deep-Sea Res. I*, 40(7), 1379-1403, 1993.

Garzoli, S.L., and M.O. Baringer, Meridional heat transport determined with expendable bathythermographs, Part II: South Atlantic transport, *Deep-Sea Res. I*, 54(8), 1402-1420, 2007.

Garzoli, S.L and R. Matano, The South Atlantic and the Atlantic Meridional Overturning Circulation, *Deep-Sea Res. II*, 58, 1837-1847, doi:10.1016/j.dsr2.2010.10.063, 2011.

Garzoli, S.,M.O. Baringer, S. Dong, R. Perez, and Q. Yao, South Atlantic meridional fluxes, *Deep-Sea Res. I,* 71, 21-32, doi:10.1016/j.dsr.2012.09.003, 2013.

Garzoli, S.L., S. Dong, R. Fine, C. Meinen, R.C. Perez, C. Schmid, E. van Sebille, and Q. Yao, The fate of the Deep Western Boundary Current in the South Atlantic, *Deep-Sea Res. I* , doi: 10.1016/j.dsr.2015.05.008, 2015.

Goni, G., S. Kamholz, S. Garzoli, and D. Olson, Dynamics of the Brazil-Malvinas Confluence based on inverted echo sounders and altimetry, *J. Geophys. Res.*, 101(C7), 16273-16289, 1996.

Goni, G. J., F. Bringas, and P. N. DiNezio, Observed low frequency variability of the Brazil Current front, *J. Geophys. Res.*, 116 (C10037), doi:10.1029/2011JC007198, 2011.

Gordon, A. L., and C. L. Greengrove, Geostrophic circulation of the Brazil-Falkland confluence, *Deep-Sea Res.*, 33(5), 573-585, 1986.

Hogg, N. G., and W. B. Owens, Direct measurement of the deep circulation within the Brazil Basin, *Deep Sea Res. II*, 46, 335-353, 1999.

Hogg, N. G., G. Siedler, and W. Zenk, Circulation and Variability at the Southern Boundary of the Brazil Basin, *J. Phys. Oceanogr.*, 29 (2), 145-157, 1999.

Hogg, N. G., and A. M. Thurnherr, A Zonal Pathway for NADW in the South Atlantic, *J. Oceanogr.*, 61(3), 493-507, doi:10.1007/s10872-005-0058-7, 2005.

Hummels, R., P. Brandt, M. Dengler, J. Fischer, M. Araujo, D. Veleda, and J. V. Durgadoo, Interannual to decadal changes in the western boundary circulation in the Atlantic at 11°S, *Geophys. Res. Lett.*, 42, 7615–7622, doi:10.1002/2015GL065254, 2015.

Johns, W.E., L. M. Beal, M. O. Baringer, J. R. Molina, S. A. Cunningham, T. Kanzow, and D. Rayner, Variability of Shallow and Deep Western Boundary Currents off the Bahamas during 2004–05: Results from the 26°N RAPID–MOC array, *J. Phys. Oceanogr.*, 38, 605–623, doi/10.1175/2007JPO3791.1, 2008.

Johns, W. E., M. O. Baringer, L. M. Beal, S. A. Cunningham, T. Kanzow, H. L. Bryden, J. J. M. Hirschi, J. Marotzke, C. S. Meinen, B. Shaw, and R. Curry, Continuous, Array-

Based Estimates of Atlantic Ocean Heat Transport at 26.5°N, *J. Clim.*, 24, 2429-2449, doi:10.1175/2010JCLI3997.1, 2011.

Latif, M., N. Keenlyside, and J. Bader, Tropical sea surface temperature, wind shear, and hurricane development, *Geophys. Res. Lett.*, 34, L01710, doi:10.1029/2006GL027969, 2007.

Lopez, H., S. Dong, S.-K. Lee, and G. Goni, Decadal Modulations of Interhemispheric Global Atmospheric Circulations and Monsoons by the South Atlantic Meridional Overturning Circulation, *J. Clim.*, 29(3), 1831-1851, doi:10.1175/JCLI-D-15-0491.1, 2016.

Lumpkin, R., and K. Speer, Large-scale vertical and horizontal circulation in the North Atlantic Ocean, *J. Phys. Oceanogr.*, 33, 1902-1920, doi:0.1175/1520-0485(2003)033<1902:LVAHCI>2.0.CO;2, 2003.

Lumpkin, R., and K. Speer, Global Ocean Meridional Overturning, *J. Phys. Oceanogr.*, 37, 2550-2562, doi:10.1175/JPO3130.1, 2007.

Lumpkin, R., and S. Garzoli, Interannual to decadal changes in the western South Atlantic's surface circulation, *J. Geophys. Res.*, 116, C01014, doi:10.1029/2010JC006285, 2011.

Majumder, S., C. Schmid, and G. Halliwell, An observations and model-based analysis of meridional transport in the South Atlantic, *J. Geophys. Res. Oceans*, 121, doi:10.1002/2016JC011693, 2016.

Masumoto, Y., H. Sasaki, T. Kagimoto, N. Komori, A. Ishida, Y. Sasai, T. Miyama, T. Motoi, H. Mitsudera, K. Takahashi, H. Sakuma, and T. Yamagata, A fifty-year Eddy resolving simulation of the world ocean – Preliminary outcomes of OFES (OGCM for the Earth simulator), *J. Earth Simulator*, 1, 3556, 2004.

Matano, R. P., On the separation of the Brazil Current from the coast, 1993, *J. Phys. Oceanogr.*, 23, 79-90, doi:10.1175/1520-0485(1993)023<0079:OTSOTB>2.0.CO;2, 1993.

McCarthy, G. D., I. D. Haigh, J. J. Hirschi, J. P. Grist, D. A. Smeed, Ocean impact on decadal Atlantic climate variability revealed by sea-level observations, *Nature,* 521, 508–510, doi:10.1038/nature14491, 2015a.

Meinen, C. S. and D. R. Watts, Calibrating Inverted Echo Sounders equipped with Pressure Sensors, *J. Atmos. Oceanic Technol.*, 15(6), 1339-1345, 1998.

Meinen, C. S. and Watts, D. R., Vertical structure and transport on a Transect across the North Atlantic Current near 42°N: Time series and mean, *J. Geophys. Res.*, 105, 21869–21892, 2000.

Meinen, C. S., Garzoli, S. L., Johns, W. E., and Baringer, M. O., Transport variability of the Deep Western Boundary Current and the Antilles Current off Abaco Island, Bahamas, *Deep-Sea Res. I*, 51, 1397–1415, 2004.

Meinen, C. S., Baringer, M. O., and Garzoli, S. L.: Variability in Deep Western Boundary Current transports: Preliminary results from 26.5°N in the Atlantic, *Geophys. Res. Lett.*, 33, L17610, doi:10.1029/2006GL026965, 2006.

Meinen, C. S., A. R. Piola, R. C. Perez, and S. L. Garzoli, Deep Western Boundary Current transport variability in the South Atlantic: Preliminary results from a pilot array at 34.5°S, *Ocean Sci.*, 8, 1041-1054, doi:10.5194/os-8-1041-2012, 2012.

Meinen, C.S., W.E. Johns, S.L. Garzoli, E. Van Sebille, D. Rayner, T. Kanzow, and M.O. Baringer, Variability of the Deep Western Boundary Current at 26.5°N during 2004-2009, *Deep-Sea Res. II*, 85, 154-168, doi:10.1016/j.dsr2.2012.07.036, 2013a.

Meinen, C, S ., S. Speich, R. C. Perez , S. Dong , A. R. Piola, S. L. Garzoli , M. O. Baringer, S. Gladyshev, and E. J. D. Campos, Temporal variability of the Meridional Overturning Circulation at 34.5°S: Results from two pilot boundary arrays in the South Atlantic, *J. Geophys. Res.-Oceans,* 118, 6461-6478, doi:10.1002/2013JC009228, 2013b.

Mémery, L., M. Arhan, X. A. Alvarez-Salgado, M.-J. Messias, H. Mercier, C. G. Castro, and A. F. Rios, The water masses along the western boundary of the south and equatorial Atlantic, *Prog. Oceanogr.*, 47, 69-98, 2000.

North, G. R., T. L. Bell, R. F. Cahalan, and F. J. Moeng, Sampling Errors in the Estimation of Empirical Orthogonal Functions, *Mon. Wea. Rev.*, 110, 699-706, 1982.

Olson, D. B., G. P. Podesta, R. H. Evans, and O. B. Brown, Temporal variations in the separation of Brazil and Malvinas Currents, *Deep-Sea Res.*, 35, 1971–1990, 1988.

Osychny, V., and P. Cornillon, Properties of Rossby Waves in the North Atlantic estimated from satellite data, *J. Phys. Oceanogr.*, 34 (1), 61-76, 2004.

Paldor, N., S. Rubin, and A. J. Mariano, A consistent theory for linear waves of the Shallow-Water equations on a rotating plane in midlatitudes, 37 (1), 115-128, doi:10.1175/JPO2986.1, 2007.

Perez, R. C., S. L. Garzoli, C. S. Meinen, and R. P. Matano, Geostrophic velocity measurement techniques for the meridional overturning circulation and meridional heat transport in the South Atlantic, *J. Atmos. Oceanic Technol.*, 28, 1504–1521, doi:10.1175/JTECH-D-11-00058.1, 2011.

970 Perez, R. C., M. O. Baringer, S. Dong, S. L. Garzoli, M. Goes, G. J. Goni, R. Lumpkin,
971 C. S. Meinen, R. Msadek, and U. Rivero, Measuring the Atlantic meridional overturning
972 circulation, *Mar. Tech. Soc. J.*, 49(2), 167-177, doi:10.4031/MTSJ.49.2.14, 2015.
973
974 Polito, P. S., and W. T. Liu, Global characterization of Rossby waves at several spectral
975 bands, *J. Geophys. Res.*, 108, 3018, doi:10.1029/2000JC000607, C1, 2003.
976
977 Polito, P. S., and O. T. Sato, Do eddies ride on Rossby waves?, *J. Geophys. Res.*, 120,
978 5417–5435, doi:10.1002/2015JC010737, 2015.
979
980 Preu, B., F. J. Hernández-Molina, R. Violante, A. R. Piola, C. M. Paterlini, T. Schwenk,
981 I. Voigt, S. Krastel, and V. Spiess, Morphosedimentary and hydrographic features of the
982 northern Argentine margin: The interplay between erosive, depositional and gravitational
983 processes and its conceptual implications, *Deep-Sea Res. I*, 75, 157-174,
984 doi:10.1016/j.dsr.2012.12.013, 2013.
985
986 Rossby, T., On monitoring depth variations of the main thermocline acoustically, *J.*
987 *Geophys. Res.*, 74, 5542–5546, 1969.
988
989 Saraceno, M., C. Provost, A. R. Piola, J. Bava, and A. Gagliardini, Brazil Malvinas
990 Frontal System as seen from 9 years of advanced very high resolution radiometer data, *J.*
991 *Geophys. Res.*, 109, C05027, doi:10.1029/2003JC002127, 2004.
992
993 Sasaki, H., M. Nonaka, Y. Sasai, H. Uehara, and H. Sakuma, An eddy-resolving hindcast
994 simulation of the quasiglobal ocean from 1950 to 2003 on the Earth simulator, in *High*
995 *Resolution Numerical Modelling of the Atmosphere and Ocean*, edited by K. Hamilton
996 and W. Ohfuchi, pp. 157–185, Springer, New York, 2008.
997
998 Schmid, C., Mean vertical and horizontal structure of the subtropical circulation in the
999 South Atlantic from three-dimensional observed velocity fields, *Deep Sea Res. I*, 91, 50-
1000 71, doi:10.1016/j.dsr.2014.04.015, 2014.
1001
1002 Schott, F.A., R. Zantopp, L. Stramma, M. Dengler, J. Fischer, and M. Wibaux,
1003 Circulation and deep-water export at the western exit of the Subpolar North Atlantic, *J.*
1004 *Phys. Oceanogr.*, 34(4), 817–843, 2004.
1005
1006 Schott, F. A., Dengler, M., Zantopp, R., Stramma, L., Fischer, J., and Brandt, P., The
1007 Shallow and deep western boundary circulation of the South Atlantic at 5–11°S, *J. Phys.*
1008 *Oceanogr.*, 35, 2031–2053, doi:10.1175/JPO2813.1, 2005.
1009
1010 Send, U., M. Lankhorst, and T. Kanzow, Observation of decadal change in the Atlantic
1011 Meridional Overturning Circulation using 10 years of continuous transport data,
1012 *Geophys. Res. Lett.*, 38, L24606, doi:10.1029/2011GL049801, 2011.
1013
1014 Smith, W. H. F., and D. T. Sandwell, Global Sea Floor Topography from Satellite
1015 Altimetry and Ship Depth Soundings, *Science*, 277 (5334), l956-1962, 1997.
1016

Srokosz, M. A., and H. L. Bryden, Observing the Atlantic Meridional Overturning Circulation yields a decade of inevitable surprises, *Science*, 348 (6241), doi:10.1126/science.1255575, 2015.

Stouffer, R. J., J. Yin, and J. M. Gregory, Investigating the causes of the response of the thermohaline circulation to past and future climate changes, *J. Clim.*, 19(8), 1365–1387, 2006.

Thompson, R. O. R. Y., Coherence Significance Levels, *J. Atmos. Sci.*, 36 (10), 2020-2021, 1979.

Toole, J. M., R. G. Curry, T. M. Joyce, M. McCartney, and B. Peña-Molino, Transport of the North Atlantic Deep Western Boundary Current about 39°N, 70°W: 2004–2008, *Deep Sea Res. II*, 58, 1768–1780, 2011.

Tracey, K. L. and Watts, D. R., On Gulf Steam meander characteristics near Cape Hatteras, *J. Geophys. Res.*, 91, 7587–7602, 1986.

Trenberth, K. E., J. M. Caron, and D. P. Stepaniak, The atmospheric energy budget and implications for surface fluxes and ocean heat transports, *Clim. Dyn*., 17, 259-276, 2001.

Van Sebille, E., Johns, W. E., and Beal, L. M., Does the vorticity flux from Agulhas rings control the zonal pathway of NADW across the South Atlantic?, *J. Geophys Res.*, 117, C05037, doi:10.1029/2011JC007684, 2012.

Vellinga, M., and R. A. Wood, Global climatic impacts of a collapse of the Atlantic thermohaline circulation, *Clim. Change*, 54(3), 251–267, 2002.

Watts, D. R., and Kontoyiannis, H., Deep-ocean bottom pressure measurement: Drift Removal and performance, *J. Atmos. Oceanic Technol.*, 7, 296–306, 1990.

Watts, D. R., and Rossby, H. T., Measuring dynamic heights with inverted echo sounders: Results from MODE, *J. Phys. Oceanogr.*, 7, 345–358, 1977.

Zangenberg N., and Siedler, G., The path of the North Atlantic Deep Water in the Brazil Basin, *J. Geophys Res.*, 103, 5419–5428, 1998.

1063
1064
1065

Tables

Site name	Instrument Type	Nominal Longitude	Nominal Latitude	Nominal Depth	Date of First Deployment
A	PIES	51° 30.0’ W	34° 30.0’ S	1360 m	March 18, 2009
AA	CPIES	50° 31.2’ W	34° 30.0’ S	2885 m	December 11, 2012
B	PIES	49° 30.0’ W	34° 30.0’ S	3535 m	March 18, 2009
BB	CPIES	48° 30.5’ W	34° 30.0’ S	4140 m	December 12, 2012
C	PIES	47° 30.0’ W	34° 30.0’ S	4540 m	March 19, 2009
D	PIES	44° 30.0’ W	34° 30.0’ S	4757 m	March 20, 2009

Table 1: Nominal locations, depths, and initial deployment dates of the PIES and CPIES moorings discussed in this paper. Note: The first instrument at Site B was a CPIES, but it was replaced with a PIES in July 2011.

	Daily	30-day low-pass filter
Mean	-15.2 Sv	-15.2 Sv
Median	-17.4 Sv	-17.4 Sv
Standard Deviation	22.8 Sv	20.3 Sv
Maximum value	+50.1 Sv	+35.0 Sv
Minimum value	-89.3 Sv	-60.8 Sv

Table 2: Statistics for the volume transport calculated from the PIES and GEM data. The transports were integrated from Site A to Site D (see Table 1) and from 800 dbar down to 4800 dbar (or the bottom, where it is shallower). Statistics were calculated over the period 2009 to 2014 using only the original PIES moorings.

Period band (days)	Variance [Sv^2]	Percentage of total variance
2 to 50	103.3 (83.1)	28.4 (25.9)
50 to 170	153.4 (61.0)	42.1 (19.0)
170 to 190	7.7 (54.9)	2.1 (17.1)
190 to 350	39.3 (54.0)	10.8 (16.8)
350 to 390	7.5 (54.9)	2.1 (17.1)
390 to record length	53.0 (12.8)	14.5 (4.0)

Table 3: Distribution of variance in the indicated period bands in the DWBC transport calculated from the PIES/CPIES observations during the continuous 2011-2014 window. The observed DWBC transport was integrated between 800 and 4800 dbar and between the original PIES at Site A and Site D. Values for transport integrated only between the PIES at Site A and Site B are shown in parentheses.

Integration span	Site A to Site D		Site A to Site B	
Integration period	2009-2014	2012-2014	2009-2014	2012-2014
Mean	-15.2 Sv	-18.0 Sv	-17.4 Sv	-17.2 Sv
Median	-17.4 Sv	-19.8 Sv	-17.2 Sv	-16.9 Sv
Standard Deviation	22.8 Sv	23.0 Sv	8.1 Sv	8.3 Sv
Maximum value	+50.1 Sv	+50.1 Sv	+18.1 Sv	+4.7 Sv
Minimum value	-89.3 Sv	-68.9 Sv	-46.5 Sv	-46.5 Sv

Table 4: Statistics for the volume transport calculated from the PIES and GEM data across the whole array (columns 2 & 3) versus only within the span between Site A and Site B (columns 4 & 5). Note that column 2 is identical to column 2 in Table 2. The transports were integrated from between the indicated sites (see Table 1) and from 800 dbar down to 4800 dbar (or the bottom where it is shallower). Statistics are shown for both the period 2009 to 2014 (columns 2 & 4) and during the enhanced array period 2012-2014 (columns 3 & 5). The transports were calculated using only the original PIES moorings; the results in the enhanced period are very similar if the CPIES are also included, as is to be expected for geostrophic calculations.

Integration span	Data mean	Data STD	Model mean	Model STD
Site A to Site B	-17.4 Sv	8.1 Sv	-17.6 Sv	7.6 Sv
Site A to Site D	-15.2 Sv	22.8 Sv	-16.0 Sv	16.5 Sv

Table 5: Time-mean and temporal standard deviation (STD) of the volume transport integrated between 800 and 4800 dbar (or the bottom where shallower) and between the indicated PIES locations. The observation-based estimates (middle columns) were calculated over the 2009-2014 time period; the model-based estimates (right two columns) were calculated over the 27-year run described in the text.

Period band (days)	Variance [Sv^2]	Percentage of total variance
6 to 50	60.0	19.2
50 to 170	105.7	33.8
170 to 190	20.8	6.7
190 to 350	56.9	18.2
350 to 390	27.3	8.7
390 to 1000	28.1	9.0
1000 to record length	13.6	4.3

Table 6: Distribution of variance in the indicated period bands in the DWBC transport calculated from the OFES model output. The model DWBC transport was integrated between 800 and 4800 dbar and between the longitudes of the real locations for the PIES at Site A and Site D.

Figures:

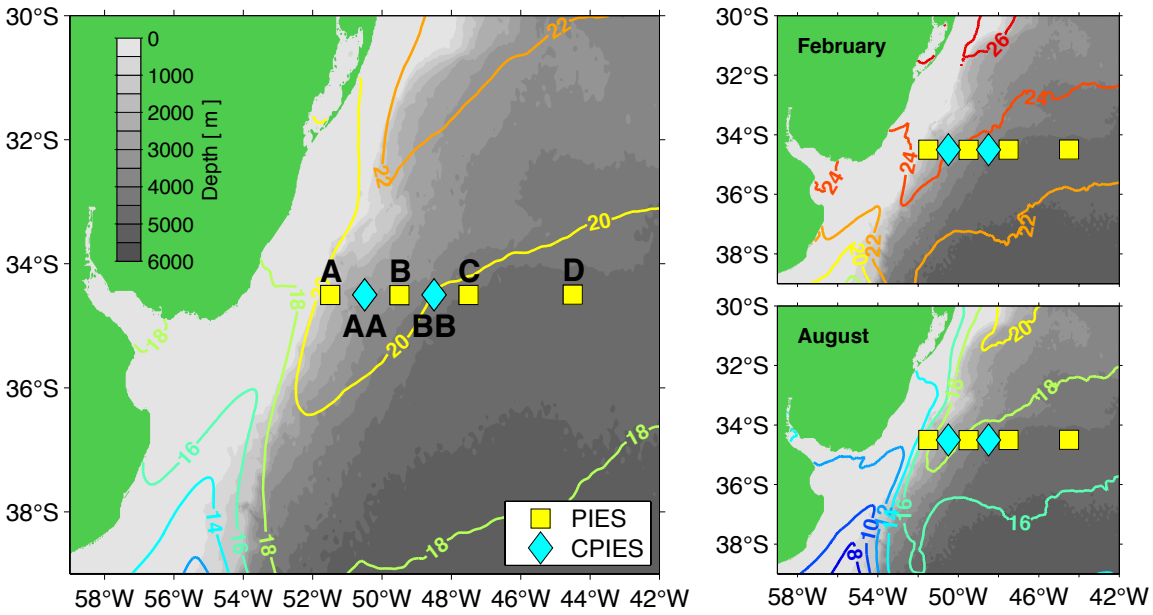

Figure 1: Map illustrating the location of the moored instruments used in this study. Instrument types are noted in the legend; site names for the original PIES (yellow squares) are "A" through "D" from west to east; the newer CPIES (cyan diamonds) site names are "AA" and "BB", also from west to east. Filled contours indicate bottom topography from the Smith and Sandwell (1997) data set. Color contours indicate the time-mean sea-surface temperature (°C) from 2009-2015 from the GHRSST MUR reanalysis SST data product (see Chin et al. 1998; see also mur.jpl.nasa.gov/multi_resolution_analysis.php). The smaller panels on the right show the monthly mean SST maps from 2009-2015 for February (top) and August (bottom) to illustrate the latitudinal range through which the Brazil-Malvinas Confluence shifts during the year.

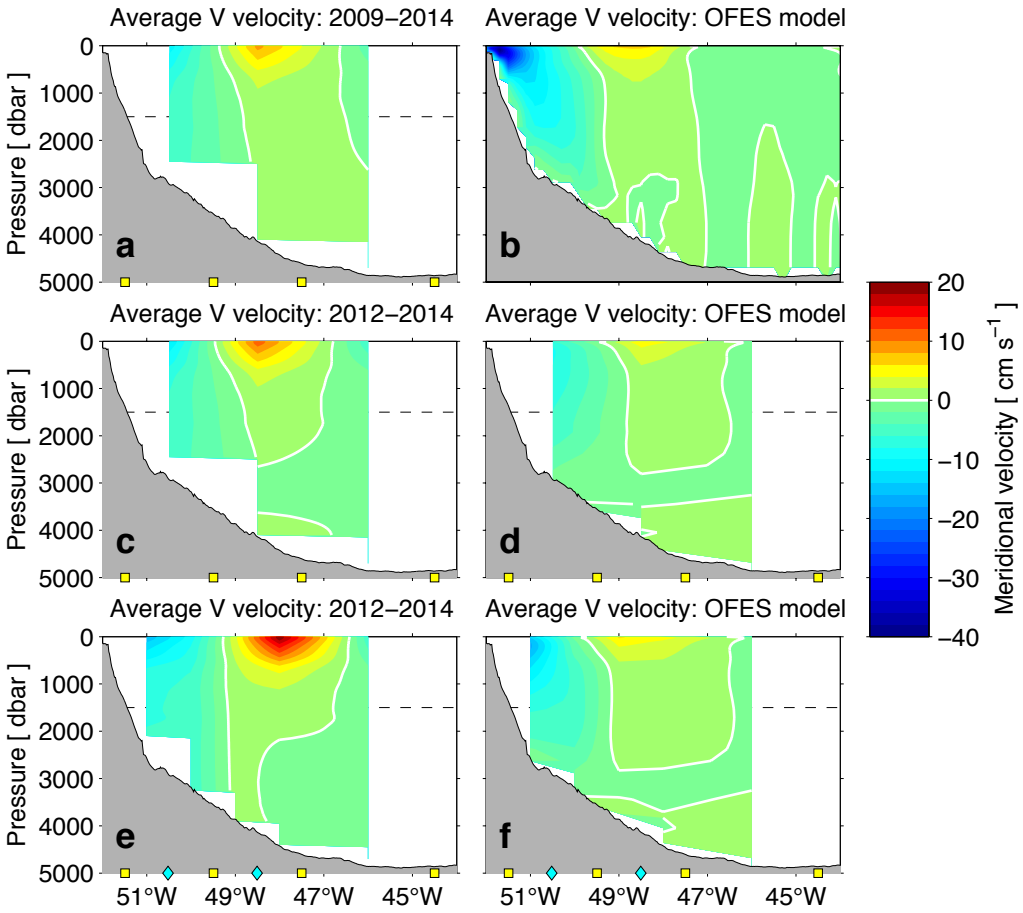

Figure 2: Time-mean meridional velocity from the PIES data (left panels) and from the OFES model (right panels). For the data-based mean sections: top panel indicates the mean over the full 5-year period for which data are available at the four PIES sites (denoted as yellow boxes on bottom axis); middle panel indicates the mean over only the ~2 years when the array was augmented, but still using only the four PIES sites; bottom panel indicates the mean over the augmented ~2 years but now using the additional CPIES sites (denoted as cyan diamonds on bottom axis). For the model-based mean sections: top panel indicates the mean at 0.2° horizontal grid resolution; middle panel indicates the time-mean with the profiles horizontally averaged between the PIES sites; bottom panel indicates the time-mean with the profiles horizontally averaged between all PIES and CPIES sites. For all panels, the gray-filled shape indicates the bottom topography from the Smith and Sandwell (1997) data set. Horizontal dashed line indicates the level where the time-mean from the model is used to reference the bottom-pressure variability. White contours in all panels indicate zero flow; color contours are at 2 cm s^{-1} intervals.

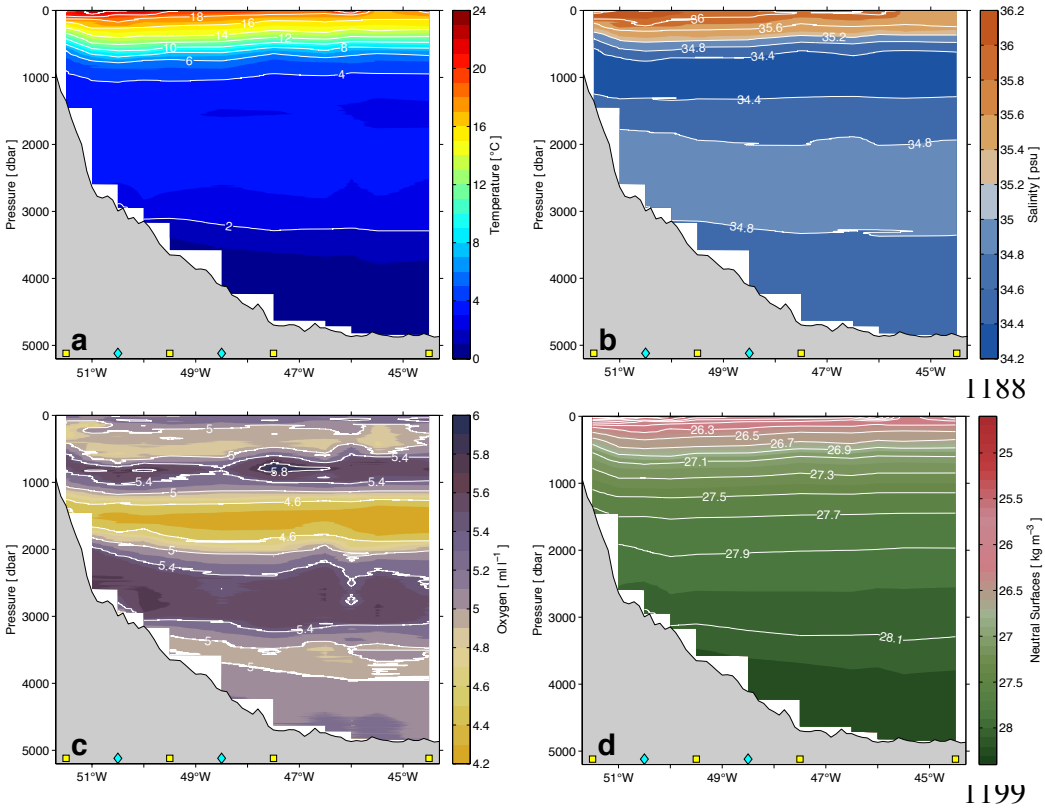

Figure 3: Average sections of in situ temperature (a), salinity (b), dissolved oxygen (c), and neutral density (d). Sections from July 2010, December 2010, July 2011, and December 2012 are averaged in a simple manner to make these plots solely to illustrate the approximate vertical distribution of the water masses in the region.

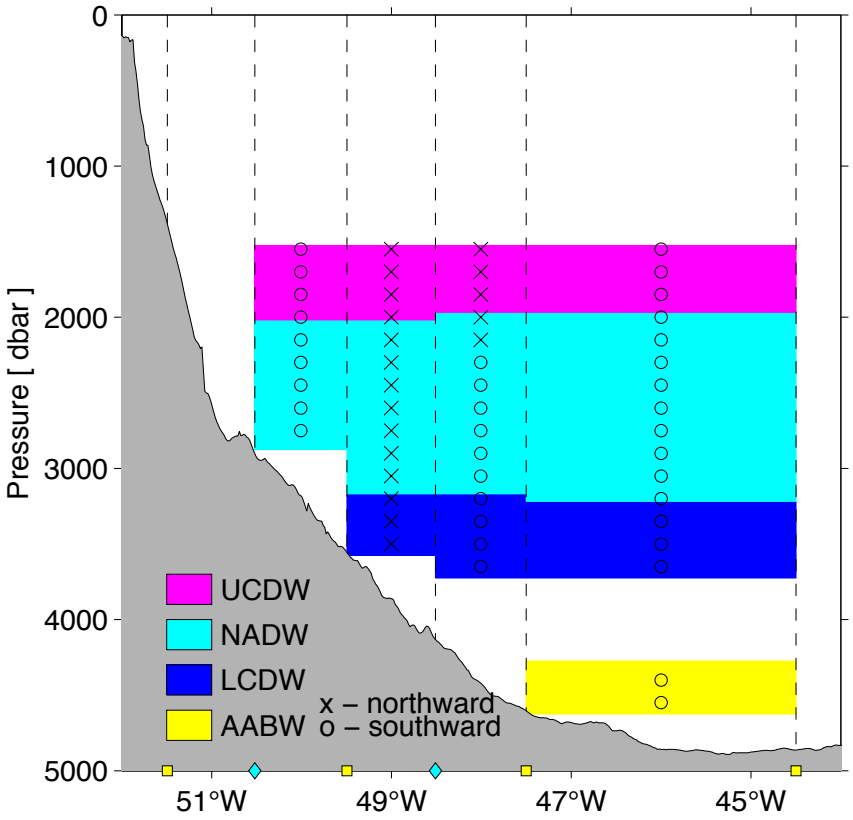

Figure 4: Schematic section illustrating the observed deep water masses and their time-mean flow direction across the section. Water mass definitions are as noted in the text, with the direction of flow denoted with either an "x" or an "o" as noted. Time-mean is determined over the December 2012-October 2014 time period when all six PIES/CPIES sites are available. Water masses are determined using the PIES+GEM estimated profiles. Note the dissolved oxygen criteria for UCDW cannot be tested using the PIES+GEM data, so only the neutral density criteria were employed here; evaluation using the CTD section data suggests that the oxygen criteria is consistently met in the depth range where the UCDW neutral density criteria are satisfied.

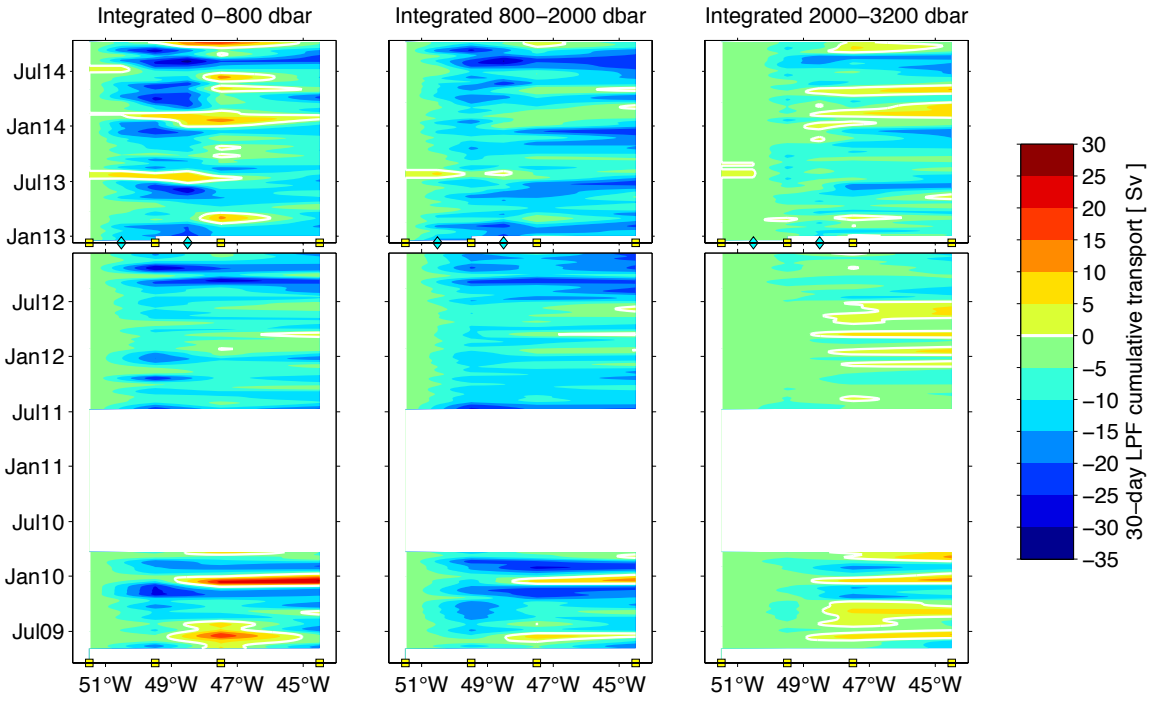

Figure 5: Hovmoller plots illustrating the 30-day low-pass filtered meridional absolute transports integrated in three layers as noted in the panel titles. Transports are cumulatively integrated offshore from the shallowest site eastward toward the center of the basin. Bold white contour indicates zero meridional flow. Symbols along the bottom axes indicate the location of the PIES and CPIES; the upper panels show the time periods when all six sites were available.

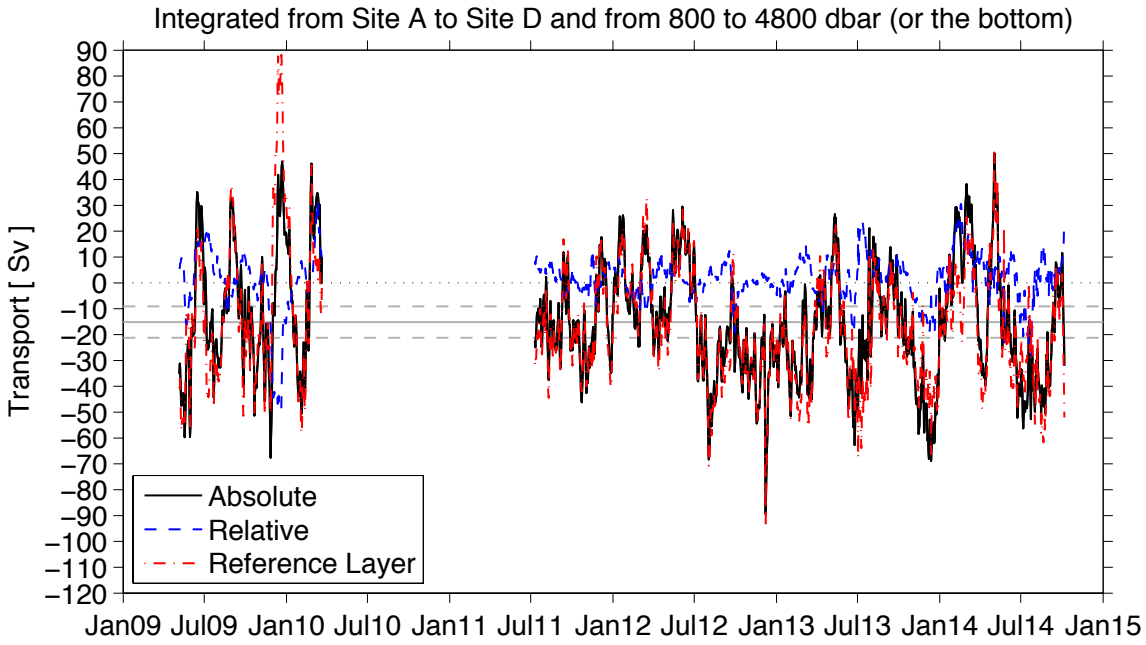

Figure 6: Time series of DWBC volume transport determined across the full horizontal span of the array and integrated vertically from 800 to 4800 dbar (or the bottom for areas where it is shallower). The total absolute transport is shown (black solid), as are the components relative to an assumed level of no motion at 800 dbar ("Relative"; blue dashed) and associated with the actual reference layer flow ("Reference Layer"; red dash-dot). The gray horizontal solid and dashed lines respectively indicate the time-mean and the time-mean plus/minus two standard errors of the mean (i.e. the 95% confidence limit for the mean value). Standard errors were determined following commonly used methods (e.g. Dewar and Bane, 1985).

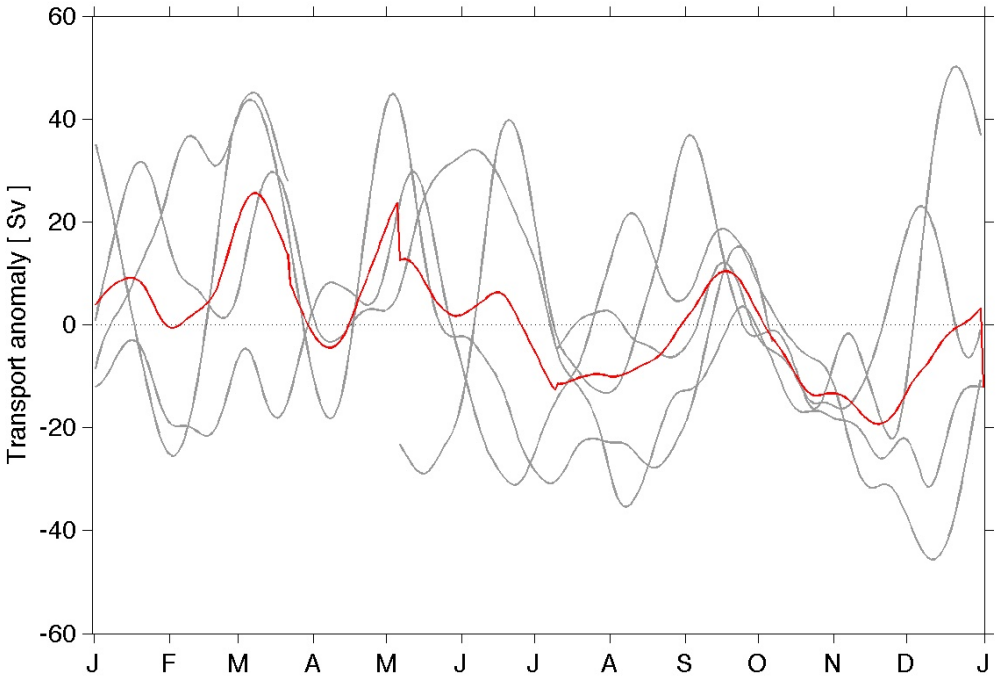

Figure 7: Annual cycle of DWBC volume transport (integrated 800-4800 dbar across the entire array); transport anomalies are shown relative to the record-length mean. Gray lines are individual years; red line is the average of all years. Transport time series was low-pass filtered with a 30-day cutoff period to reduce the higher frequency signals.

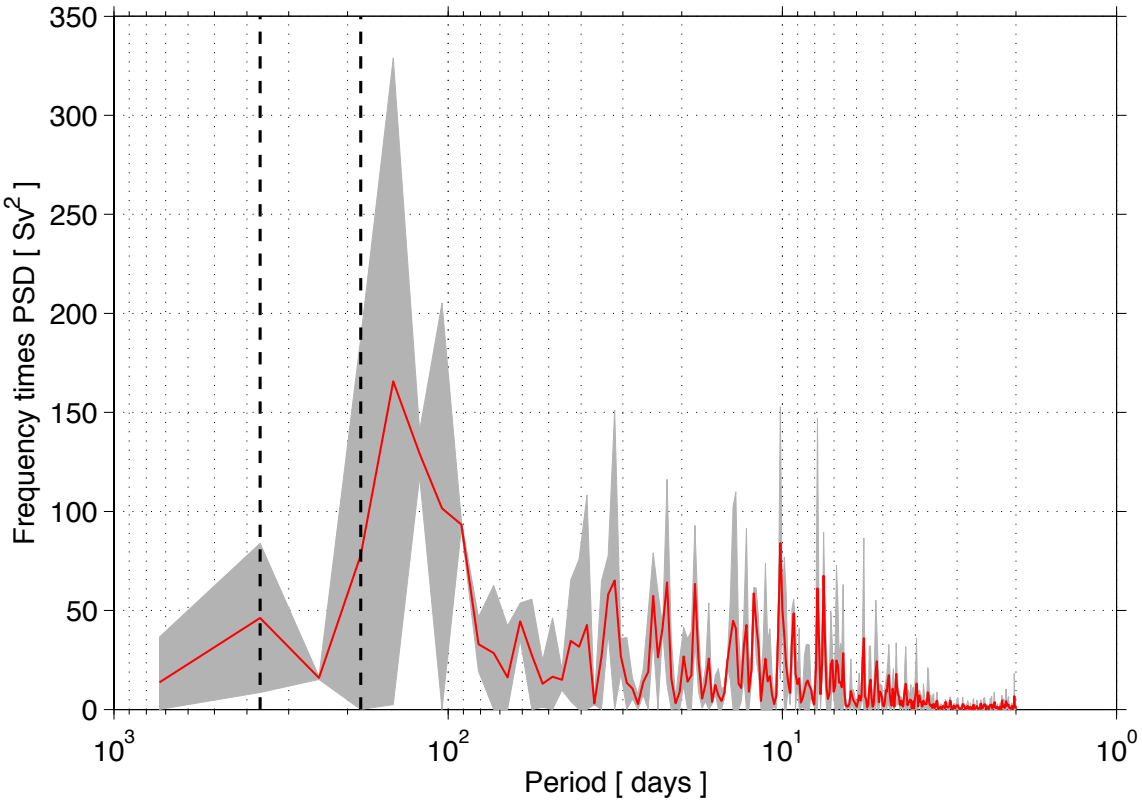

Figure 8: Variance preserving spectrum of the DWBC volume transport using the continuous record that begins in July 2011. Spectrum determined using Welch's averaged periodogram method and a 2-year window allowing 1-year of overlap. Gray shading indicates the 95% confidence limits. Vertical black dashed lines indicate the annual and semi-annual periods.

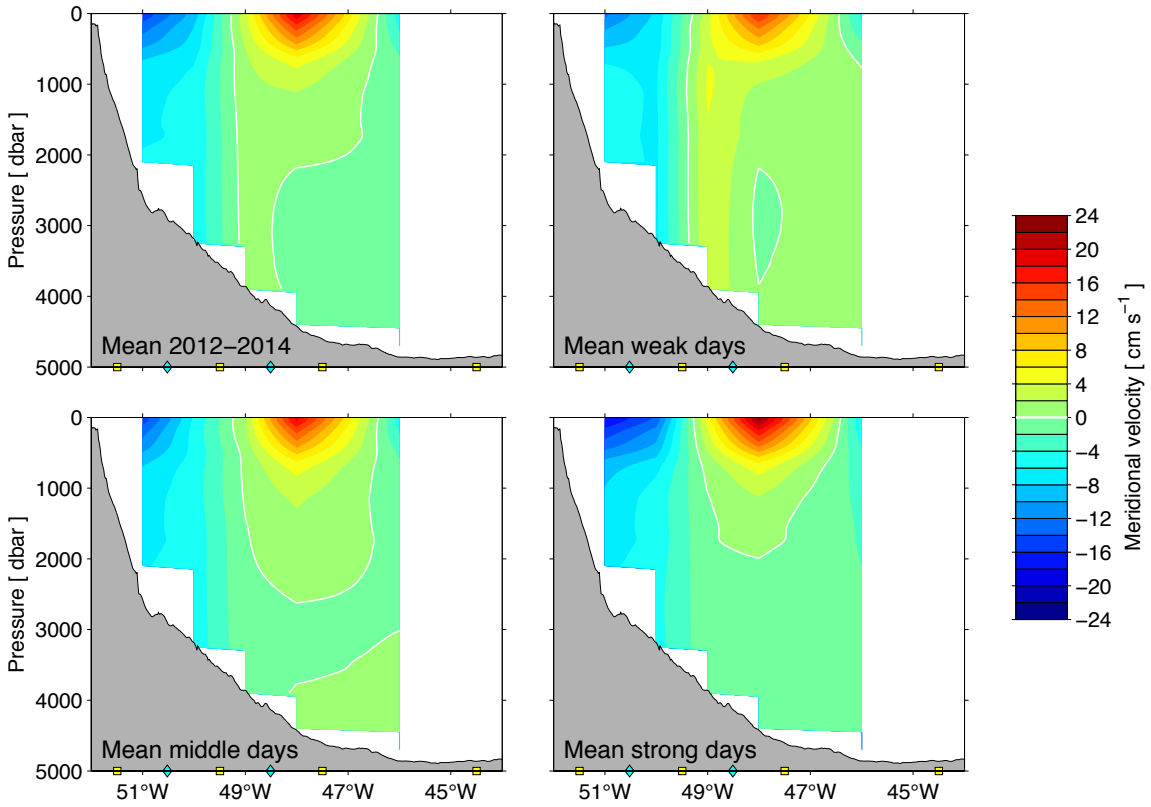

Figure 9: Composite meridional velocity sections based on the average of all data when the enhanced array is in place, December 2012-October 2014 (top left); the average of all days when the southward DWBC transport is within ± 2 standard errors around the mean value ("middle" – lower left); the average of the days where the southward DWBC transport is weaker than the mean minus 2 standard errors ("weak" – top right); and the average of the days where the southward DWBC transport is stronger than the mean plus 2 standard errors ("strong" – lower right). Gray shading indicates bottom topography; symbols along bottom of each panel indicate the PIES and CPIES sites. Note the color bar range is different than for Figure 2. White contours in all panels indicate zero flow.

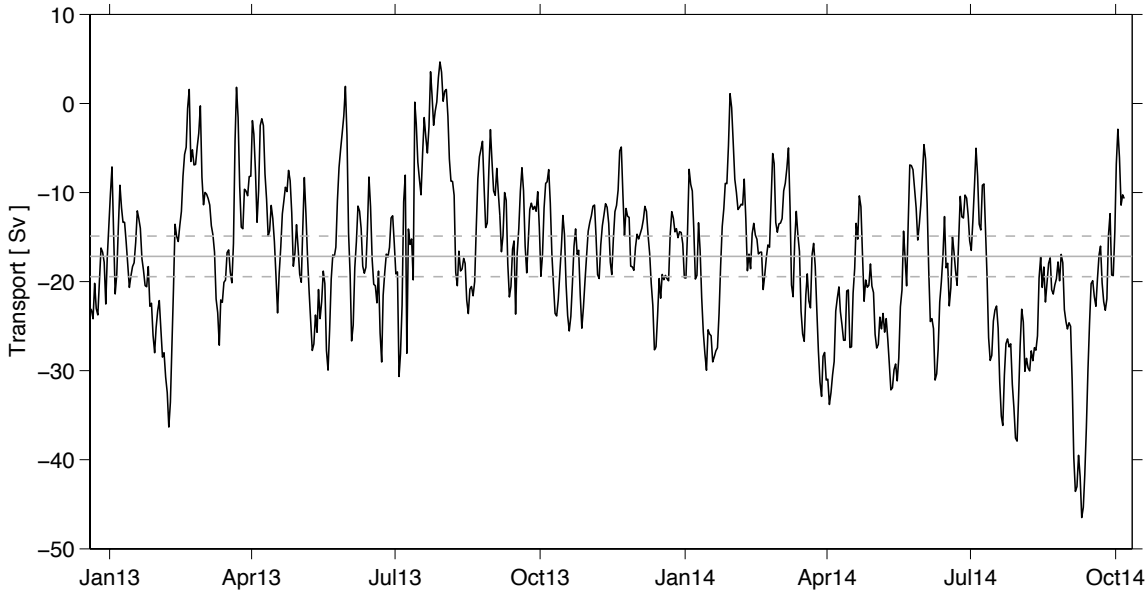

Figure 10: Time series of absolute transport integrated between Sites A and B, and between 800 dbar and 4800 dbar (or the bottom), during the period when all instruments were in place. Also shown is the time-mean value (gray solid line) and lines corresponding to the time-mean plus or minus two standard errors of the mean (gray dashed), i.e. the 95% confidence limit for the mean value. Standard errors were determined following commonly used methods (e.g. Dewar and Bane, 1985).

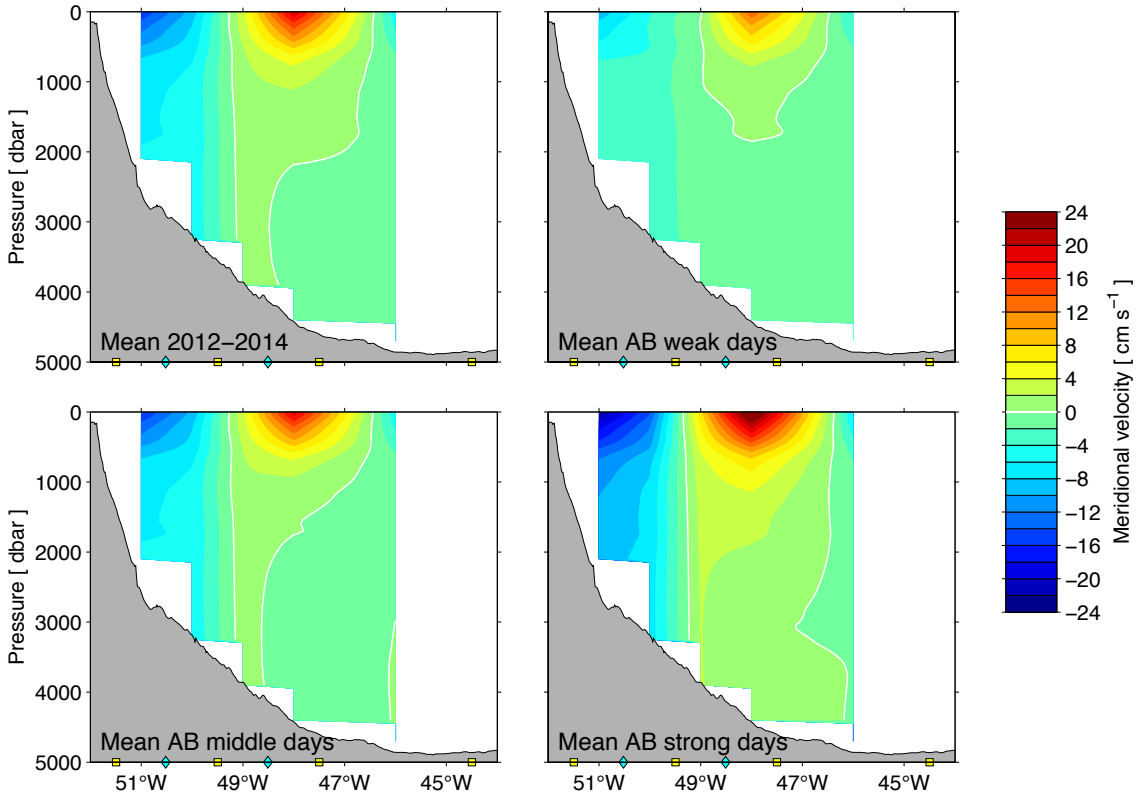

Figure 11: Same as Figure 9, except that the transport time series used for identifying strong and weak southward transport days was integrated only between Sites A and B (i.e. the record in Figure 10) instead of between Sites A and D. White contours in all panels indicate zero flow.

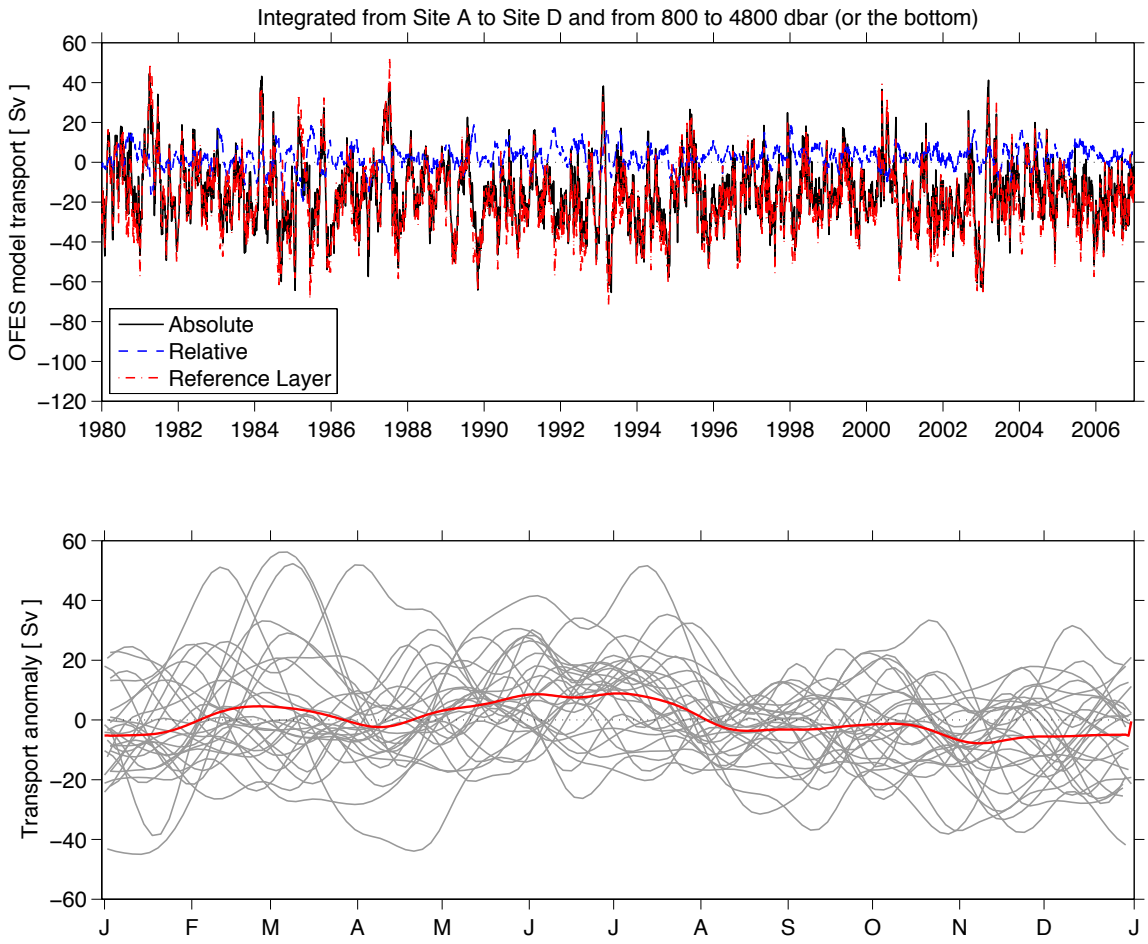

Figure 12: Time series of DWBC volume transport calculated from output of the OFES numerical model run described within the text. Transport was integrated within 800 to 4800 dbar and between the longitudes of the real world PIES at Sites A and D. Top panel: the complete time series of absolute transport, with the every-three-day full resolution, is shown as the black solid line, while the relative and reference contributions calculated as in Figure 6 are shown in blue dashed and red dash-dot lines, respectively. Bottom panel: annual cycle of the model DWBC transport anomaly, calculated and shown in the same manner as for the observational record shown in Figure 7.

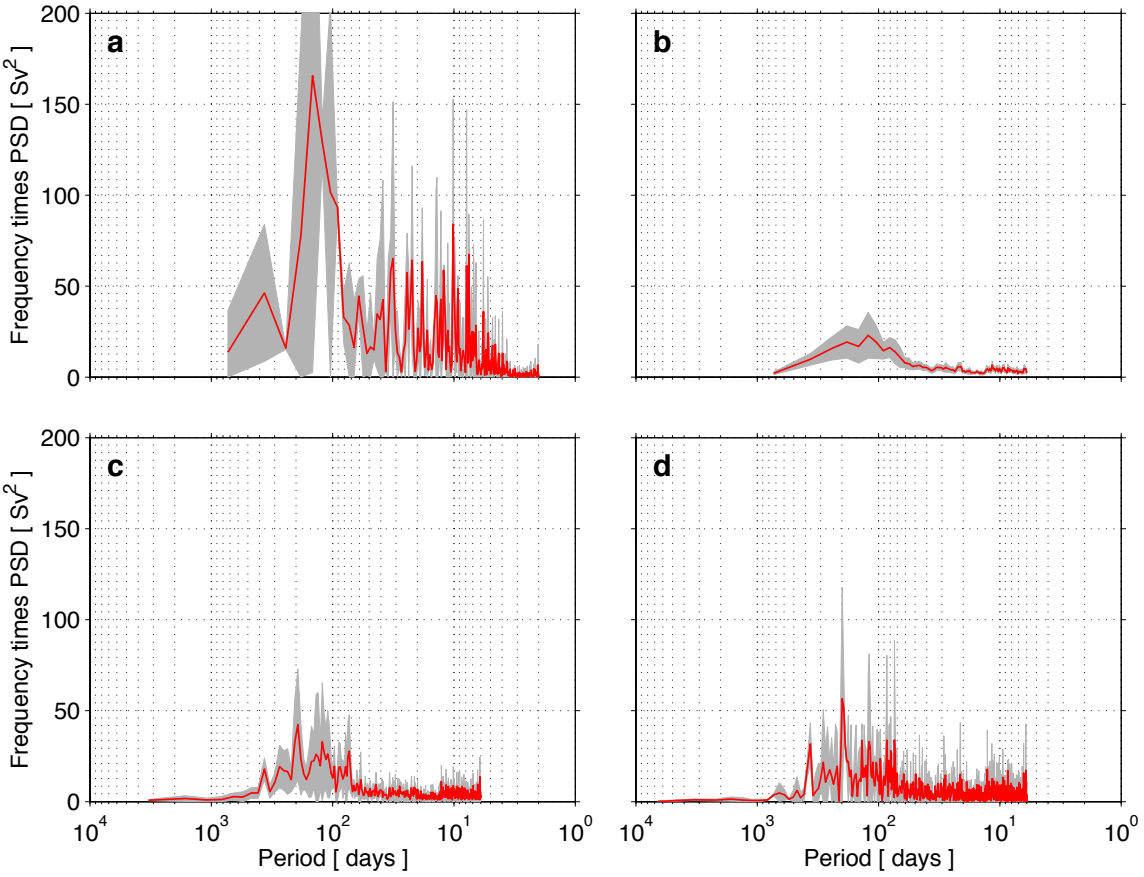

Figure 13: Variance preserving spectra of the DWBC volume transport time series (integrated from 800 to 4800 dbar and between PIES Sites A and D). a) Spectrum for the observational record – as in Figure 8 but restricting the y-axis range for comparison purposes. b) Spectrum for the DWBC transport calculated from the OFES numerical model output within the same pressure/longitude bounds and utilizing a two-year window length with 50% window overlap. c) Same as panel b but using a nine-year window length with 50% window overlap. d) Same as panel b but using an eighteen-year window length with 50% window overlap. For all panels the gray shaded region represents the 95% confidence limits for the calculated spectrum. All spectra determined using the Welch's averaged periodogram method.

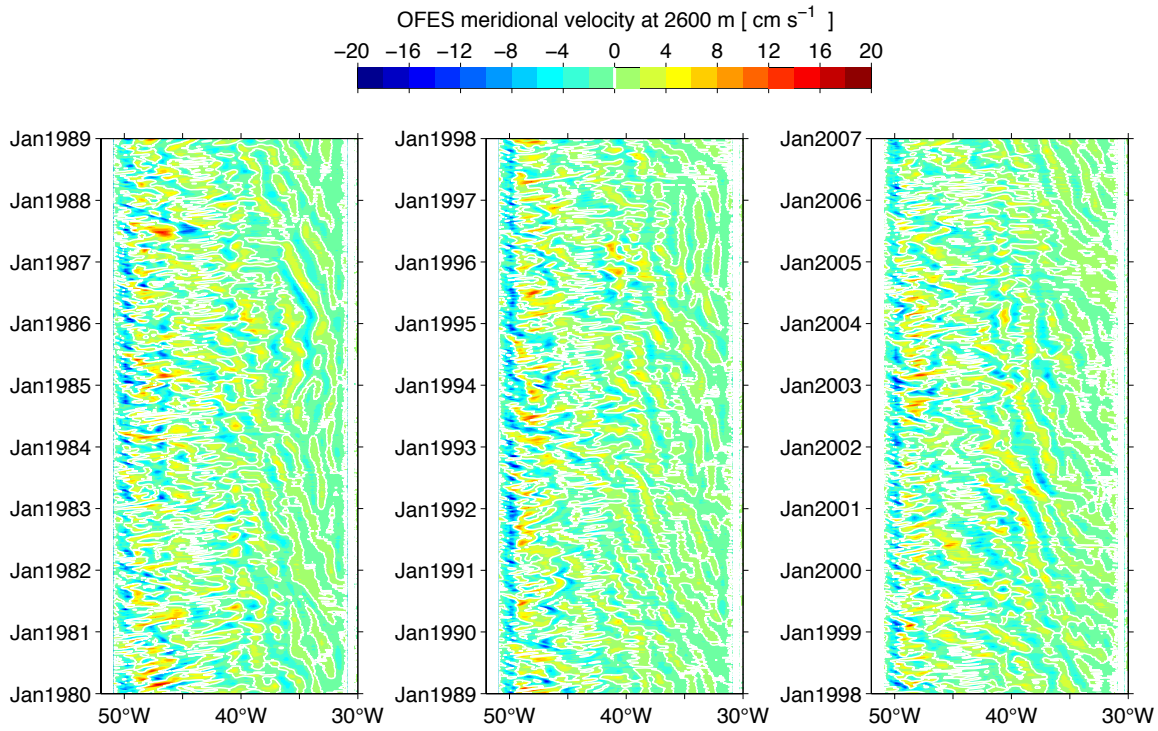

Figure 14: Hovmoller plot illustrating the OFES model meridional velocity along 34.5°S at the core of the NADW near 2600 m depth. Velocities are shown for the final 27 years of the run discussed in the text, broken into three 9-year panels. White contours indicate zero flow.

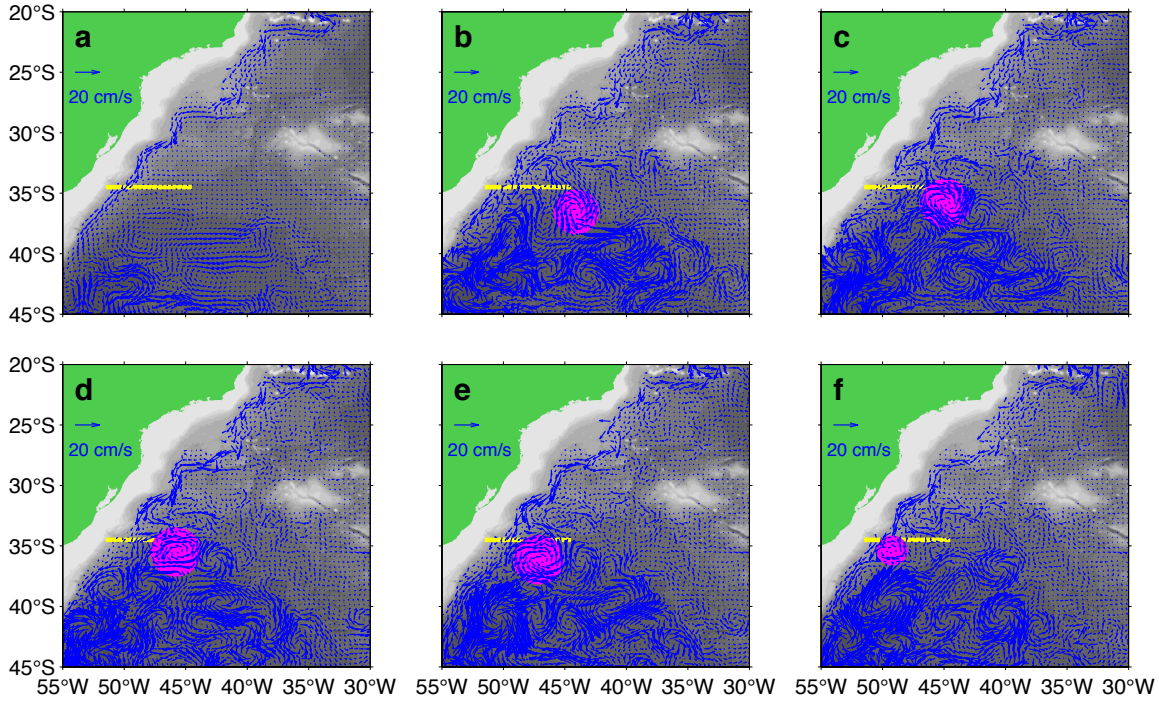

Figure 15: Velocities from the OFES model at the core of the NADW near 2600 m depth: (a) average over the full 27-year run described in the text; (b) average over August 1987; (c) average over September 1987; (d) average over October 1987; (e) average over November 1987; (f) average over December 1987. Land is denoted by green; bottom topography is from the Smith and Sandwell (1997) data set. Yellow line denotes nominal location of the PIES/CPIES array in the real ocean. Magenta disc highlights the propagating eddy/wave feature discussed in the text.